

Title: Observed declines in upper ocean phosphate-to-nitrate availability

Authors: Skylar D. Gerace¹, Jun Yu¹, J. Keith Moore¹, Adam C. Martiny^{1,2*}

Affiliations:

¹Department of Earth System Science, University of California, Irvine; Irvine, 92697, United States of America.

²Department of Ecology and Evolutionary Biology, University of California, Irvine; Irvine, 92697, United States of America.

*Corresponding author. Email: amartiny@uci.edu

Abstract:

Climate warming is increasing ocean stratification, which in turn should decrease the flux of nutrients to the upper ocean. This may slow marine primary productivity, causing cascading effects throughout food webs. However, observing changes in nutrient concentrations at the ocean surface is challenging because they are often below detection limits. The nutricline depth, where nutrient concentrations reach well-detected levels, is related with productivity and indicates upper ocean nutrient availability. Here, we quantified nutricline depths from a global database of observed vertical nitrate and phosphate profiles (1972 - 2022) to assess contemporary trends in global nutrient availability. We found strong evidence that the P-nutricline (phosphacline) is mostly deepening, especially throughout the southern hemisphere, but the N-nutricline (nitracline) remains mostly stable. Earth System Model simulations support the hypothesis that reduced iron stress and increased nitrogen fixation buffer the nitracline, but

not phosphacline, against increasing stratification. These contemporary trends are expected to continue in the coming decades, leading to increasing phosphorus but not nitrogen stress for marine phytoplankton, with important ramifications for ocean biogeochemistry and food web dynamics.

5

Main Text:

Nitrate and phosphate are key nutrients for ocean ecosystems (1), and Earth System Models (ESMs) predict that increasing ocean stratification due to climate warming is decreasing upper ocean nutrient supply (2 - 4). This trend can substantially reduce phytoplankton productivity, and in turn negatively impact marine food webs (5). Consistent with these predictions, climate-induced declines of the nutrient supply coincide with reduced productivity throughout the geological record (6, 7). Despite these predictions, the expected decline in present-day surface nutrient availability has yet to be detected.

A major challenge with observing contemporary changes in nitrate and phosphate is that they are often below detection limits throughout the ocean surface (8, 9). However, both nutrients increase with depth (10). The nutricline depth, where either nutrient first reaches a well-detected concentration, commonly occurs below the surface where light limits photosynthesis and remineralized nutrients accumulate (11, 12). This depth is widely recognized as a proxy for nutrient availability due to its relationships with phytoplankton productivity (13), resource demand (14), and community composition (15). Additionally, the nutricline depth is intimately linked with stratification, as a more stratified ocean typically exhibits weaker vertical mixing and reduced nutrient flux rates (16). Therefore, nutricline depths may proxy upper ocean nutrient availability

at a global scale, and we hypothesize that ongoing stratification has deepened nutricline depths worldwide in recent decades.

We quantified nutricline depths from 1972 to 2022 throughout the global ocean and evaluated their accuracy as a proxy for global nutrient limitation. Our core analysis included 31,715 nitrate and 5 phosphate depth profiles measured using standardized analytical techniques by the Global Ocean Ship-based Hydrographic Investigations Program (GO-SHIP). Nutricline depths for nitrate (nitracline, Z_{NO_3}) and phosphate (phosphacline, Z_{PO_4}) were defined from threshold concentrations in Redfield proportions ($[NO_3^-] = 3 \mu\text{mol kg}^{-1}$ & $[PO_4^{3-}] = 3/16 \mu\text{mol kg}^{-1}$) (17). Spatially, mean 10 nutracline and phosphacline depths are deepest in areas with the lowest surface concentrations, and when high nutrient stress was detected by bioassay experiments and genetic biomarkers (18, 19) 15 (Fig. 1 and Fig. S1). Deep nutriclines are predominantly found at low and middle latitudes (Fig. 1A,B), in agreement with the notion that oligotrophic waters are mostly within tropical and subtropical regions (20). The phosphacline is only deeper than the nitracline in the North Atlantic 20 subtropical gyre and Mediterranean Sea (Fig. 1C), which are known P-stressed regions (21 - 23). There is also an east-west phosphacline vs. nitracline gradient in the North Pacific Ocean matching changes in sparse surface phosphate concentrations measured with high sensitivity techniques (9). The nitracline is much deeper than the phosphacline in each of the southern subtropical gyres (Fig. 1C). We found that nutricline depths from two larger, but more heterogeneous data sets (Global Ocean Data Analysis Project [GLODAP] and World Ocean Database [WOD]), have nearly identical spatial distributions to the depths obtained using data from GO-SHIP (Fig. S2). In summary, these spatial patterns suggest that nutricline depths can serve as an effective proxy for the large-scale distribution of nutrient availability and stress throughout the upper ocean.

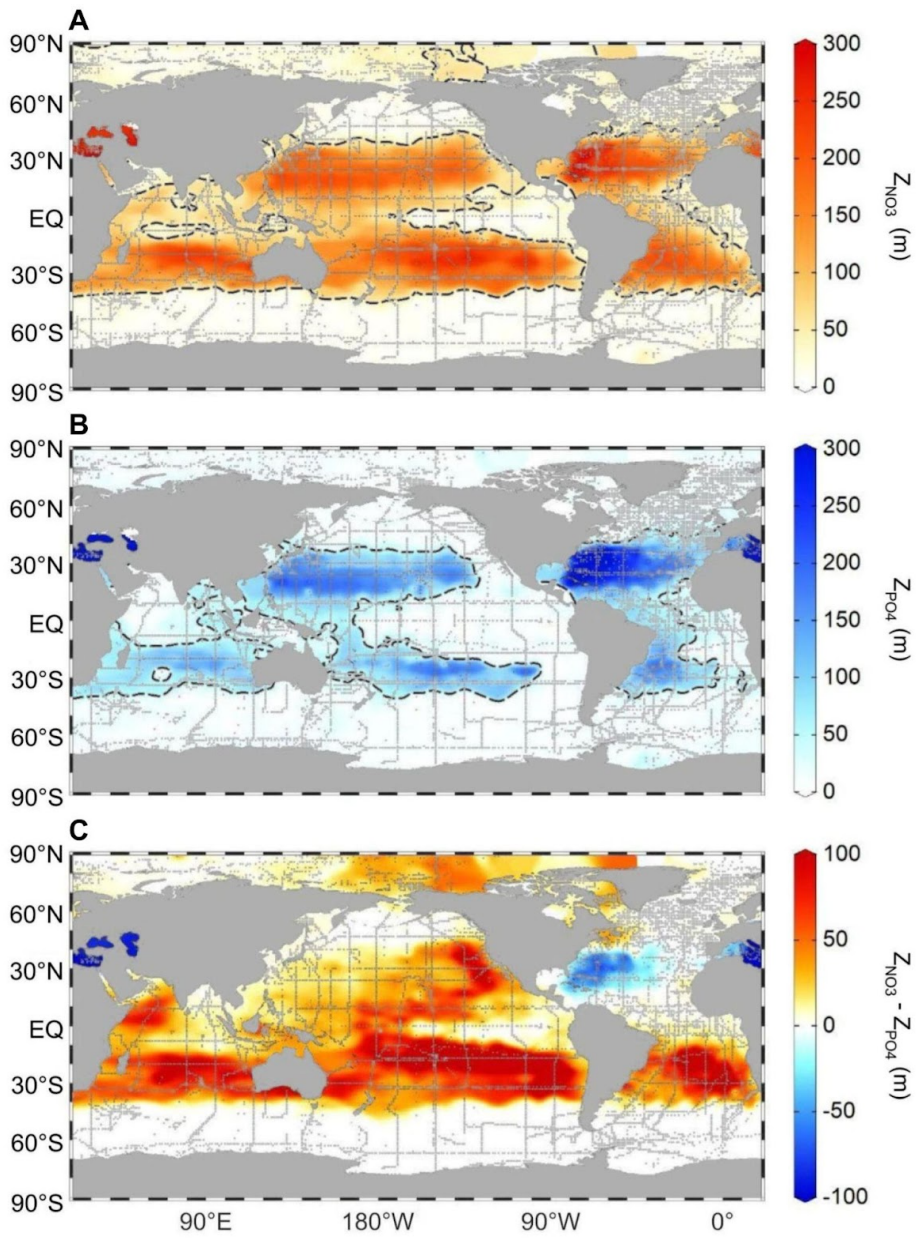


Figure 1: Mean nutricline depths were consistent with patterns of nutrient availability and limitation. This figure depicts nutricline depths from GO-SHIP. (A) Nitractine depths (Z_{NO_3}) and (B) phosphactine depths (Z_{PO_4}) depicted here are average values for all of 1972 - 2022 at each unique geographic coordinate (gray dots; sites for Z_{NO_3} , $n = 8,508$; sites for Z_{PO_4} , $n = 9,033$). The thresholds for defining these nutricline depths were $3 \mu\text{mol kg}^{-1}$ and $3/16 \mu\text{mol kg}^{-1}$ for nitrate and phosphate respectively. The dashed line is the contour of 50 m depth; we determined trends from nutriclines deeper than 50 m. (C) The difference of average nitractine and phosphactine depths (sites for $Z_{NO_3} - Z_{PO_4}$, $n = 8,284$). These maps show values that were spatially interpolated using DIVA in Ocean Data View.

5

Nutricline trends revealed declining phosphate-to-nitrate availability

To test our hypothesis of a deepening nutricline, we estimated the temporal trends for the annually averaged nitracline and phosphacline depths using two separate linear regressions (Fig. S3). The
5 nitracline regression shows no significant change over time ($p = 0.07$). However, the phosphacline significantly deepened ($p = 9 \times 10^{-7}$) by 23 m over the past 5 decades (T_{PO_4} slope = 0.47 m yr^{-1} , slope SE = 0.10 m yr^{-1}) (Fig. S3A,B and Table S1). To put this rate into perspective, the average phosphacline depth in southern oligotrophic waters (45°S to 1°S) is only 62 m, and the average difference between the nitracline and phosphacline depths ($Z_{NO_3} - Z_{PO_4}$) is only 31 m throughout
10 the global oligotrophic ocean (45°S to 45°N) (Table S2). To account for seasonality in sampling, we corrected observed nutricline depths by subtracting their respective monthly climatological value. Again, only the phosphacline exhibits a deepening trend, whereas the nitracline displays no temporal trend (Fig. S3C-E). However, using different global data sets or threshold concentrations does sometimes indicate nitracline deepening, although this deepening rate never exceeds the rate
15 for phosphacline depths (Table S1). Also, nitracline and phosphacline slopes were not significantly different for the lowest threshold concentrations, likely due to poorly resolved phosphacline depths at these low concentrations. Nonetheless, these global regressions consistently show that the phosphacline is deepening faster than the nitracline.

20 We next quantified site-specific trends for the nitracline (T_{NO_3}) and phosphacline (T_{PO_4}) depths (Fig. 2 and Table S3). This was done to eliminate the possibility that the spatiotemporal variability in sampling induced a spurious trend by over-representing locations with particularly deep nutriclines at later years. The median T_{NO_3} was negative (-0.11 m yr^{-1} , CI_{95%} = [-0.22, -0.02]) indicating a possible shoaling. In contrast, the median T_{PO_4} shows a greater inclination for

phosphacline deepening (0.35 m yr^{-1} , CI_{95%} = [0.20, 0.49]). Similar with the global regression, this suggests a general deepening of the phosphacline at a rate of 18 m over the past 50 years. Thus, the site-specific trends show that only the phosphacline is deepening, whereas the nitracline is stable or could even be shoaling.

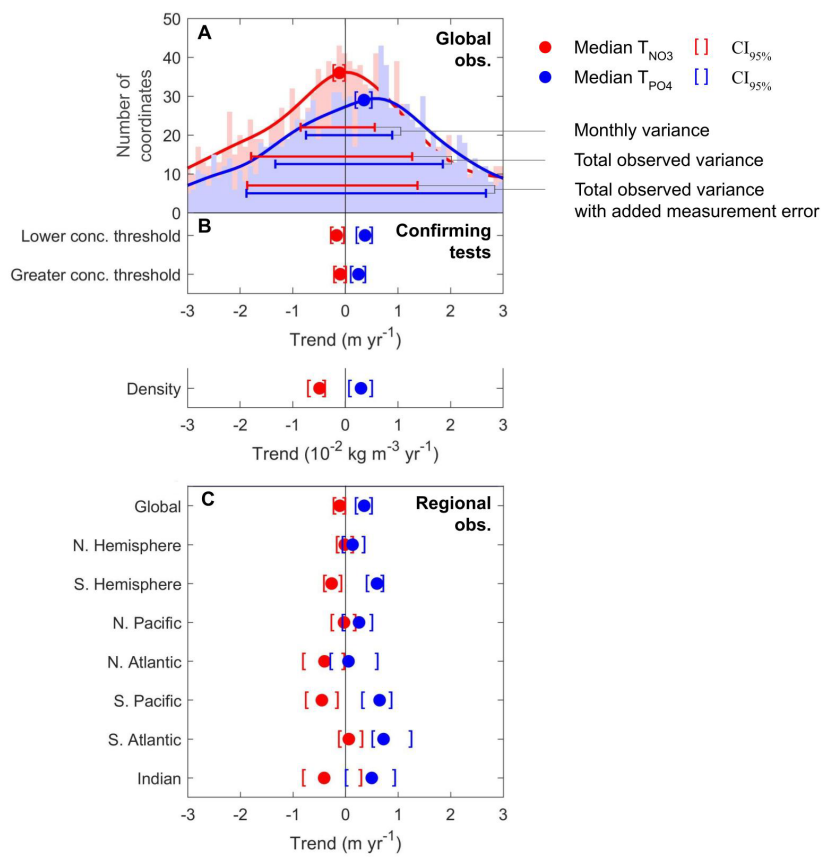


Figure 2: Nutricline trends revealed declining phosphate-to-nitrate supply worldwide. Nutricline depths were defined based on threshold concentrations of $[NO_3^-] = 3 \mu\text{mol kg}^{-1}$ and $[PO_4^{3-}] = 3/16 \mu\text{mol kg}^{-1}$. **(A)** Site-specific trends for each geographic coordinate (sites for T_{NO_3} , $n = 1,859$; sites for T_{PO_4} , $n = 1,641$). 95% confidence intervals ($CI_{95\%}$) were calculated for each median trend by finding 10,000 bootstrap samples of the respective data set. The curves over the histograms depict the kernel densities. The sets of error bars from top to bottom are the interquartile ranges of T_{NO_3} and T_{PO_4} from the WOA18 monthly climatology, GO-SHIP observations, and GO-SHIP observations with added measurement error. **(B)** Medians of T_{NO_3} and T_{PO_4} when defining nutricline depths based on lower ($[NO_3^-] = 1 \mu\text{mol kg}^{-1}$ and $[PO_4^{3-}] = 1/16 \mu\text{mol kg}^{-1}$) and higher ($[NO_3^-] = 5 \mu\text{mol kg}^{-1}$ and $[PO_4^{3-}] = 5/16 \mu\text{mol kg}^{-1}$) threshold concentrations. Additionally, the global density trends of nutricline depths. See Table S3 for detailed statistics of these observed trends. **(C)** Regional medians of T_{NO_3} and T_{PO_4} . See Table S4 for detailed descriptions of these regions and their respective statistics.

We also observed extensive variability among site-specific trends (Fig. 2A), including both deepening and shoaling nutriclines across smaller ocean regions. Multiple mechanisms, including seasonality, likely contribute to the observed variation among sites. However, we will next show
5 that none of the tested mechanisms can account for the long-term deepening in the phosphacline, but not nitracline. Simulating the actual sampling dates onto a fixed monthly climatology (WOA18 with no long-term change) resulted in interquartile ranges of T_{NO_3} and T_{PO_4} that are about 50% of the observed variances. This suggests that monthly variability in nutrient concentrations is an important source of variation in site-specific trends (Fig. 2A and Fig. S4C,D). Next, we constructed
10 10,000 random populations of the fixed monthly climatology to robustly quantify the effect of seasonal variance without any long-term changes (Fig. S4E,F). The median trends in nutricline depths are indistinguishable from zero, showing that monthly variability does not lead to an overall bias in median trends. We then introduced an artificial fixed long-term trend at all sites in the random populations. This resulted in the same variance with different locations showing a mix of
15 deepening or shoaling trends in agreement to what we found in the actual observations. However, the median shifted to match the fixed imposed trend (Fig. S4G,H). We interpret these analyses as the observed median capturing the actual underlying tendency in trends, whereas the variance in site-specific trends is mostly attributed to seasonality. To match both the observed median trends and overall variance in depths, each nitracline trend had to be sampled from a normal distribution
20 with a shoaling tendency (mean = -0.63 m yr⁻¹, SD = 1.5 m yr⁻¹), and each phosphacline trend came from one with a deepening tendency (mean = 0.20 m yr⁻¹, SD = 1.0 m yr⁻¹) (Fig. S4I,J). This demonstrates that the median trend robustly captures the underlying tendency of the site-specific trends despite their high variability. In summary, these analyses show that sampling timing contributes to the observed variability in trends between sites, but any overall shift in the median must come from a long-term change in nutricline depths.

Outside of seasonality, variability in the site-specific trends could also arise from measurement error or interannual climate forcings. When we simulated measurement uncertainty to the observed nutrient concentrations, we found that the interquartile range of T_{NO_3} only increased about 5% (Fig. 2A). In contrast, the interquartile range of T_{PO_4} increased about 40% due to the low threshold concentration (Fig. 2A). This suggests that measurement error is a considerable factor for the variability of T_{PO_4} but not T_{NO_3} , despite both having nearly equal total variance. However, accounting for sampling error to nutrient concentrations still yielded a median T_{NO_3} indicative of shoaling, and a median T_{PO_4} indicative of deepening (median $T_{NO_3} = -0.18 \text{ m yr}^{-1}$, $CI_{95\%} = [-0.27, -0.03]$; median $T_{PO_4} = 0.26 \text{ m yr}^{-1}$, $CI_{95\%} = [0.09, 0.43]$). Part of the total variance could also be attributed to ENSO or other climate modes, which can affect upper ocean nutrient profiles on interannual timescales (24). We found that during some El Niño years, the global median nitracline and phosphacline depths were relatively deeper (Fig. S5). Thus, the combination of seasonal and interannual changes in nutrient concentrations together with measurement uncertainty explain most of the observed variance in nutricline trends.

Despite a large variability, the median values of T_{NO_3} and T_{PO_4} are both significantly different from zero and from each other. To confirm this, we scrambled the sampling time to construct 10,000 randomized conglomerate data sets and found the median trends for each of these random populations (MToRP). This showed that the probabilities of the observed medians in T_{NO_3} and T_{PO_4} being zero are less than 2×10^{-2} and 1×10^{-5} respectively when compared to 10,000 randomized data sets (Table S3). Moreover, sign and Kruskal-Wallis tests also supported that both median trends are significantly different from zero and each other (Table S3). Thus, there is some support for a shoaling of the nitracline, and strong support for a deepening of the phosphacline.

The median trends are also consistent across different observational products and choice of threshold concentrations (Fig. 2B and Table S3). WOD hosts nearly an order of magnitude more nutrient observations than GO-SHIP, but these observations were collected with a diversity of protocols. Nonetheless, WOD similarly shows overall shoaling and deepening trends of the nitracline and phosphacline, respectively (Table S3). The GLODAPv2.2022 adjusted product also shows that any measurement bias with time has little influence on the median trends (Table S3). Additionally, we defined nutricline depths using different threshold concentrations and found similar medians for site-specific trends through time (Table S3). Therefore, the median trends across different databases and definitions agree that phosphacline depths are mostly deepening, whereas nitracline depths are mostly shoaling (Fig. 2B and Table S3).

We finally explored the robustness of the median trends with a variety of additional tests. First, we found a negative median trend for the paired residual $Z_{\text{NO}_3} - Z_{\text{PO}_4}$, which also suggests a faster deepening of the phosphacline relative to the nitracline (Fig. S6). Second, there was no indication of a bias due to changing measurement methods during the observation period. After subtracting mean climatological concentrations, we saw no negative trend at depths well below the nutricline where concentrations presumably should be stable (Fig. S7). Third, the water density at the depth of the nitracline and phosphacline show decreasing and increasing trends respectively (median $T_{\text{NO}_3} = -5 \times 10^{-3} \text{ kg m}^{-3} \text{ yr}^{-1}$, $\text{CI}_{95\%} = [-7 \times 10^{-3}, -4 \times 10^{-3}]$; median $T_{\text{PO}_4} = 3 \times 10^{-3} \text{ kg m}^{-3} \text{ yr}^{-1}$, $\text{CI}_{95\%} = [8 \times 10^{-4}, 5 \times 10^{-3}]$; Fig. 2B). This indicates that the nutricline depths are shifting independently of density layers, suggesting that biological processes may control the nutricline depth trends.

Based on the combination of these tests and analyses, we conclude that there is strong support for a general deepening of the phosphacline. It is less certain if the nitracline is stable or possibly shoaling, but it is clearly not deepening as fast as the phosphacline. Thus, our analysis points to differential shifts in nutricline depths for these two nutrients, revealing a contemporary depletion of upper ocean phosphate relative to nitrate.

5

A hemispherical difference in nutricline trends

A regional analysis revealed a significant hemispheric difference in the observed nutricline trends (Fig. 2C and Table S4). Neither nutricline depths show any significant trends in the northern hemisphere. If we split the northern hemisphere into basins, the median T_{NO_3} is significantly negative (shoaling) in the North Atlantic, whereas the median T_{PO_4} is marginally positive (deepening) in the North Pacific. Across the southern hemisphere, the median trends are indicative of phosphacline deepening and nitracline shoaling, although the medians are not significant for the Indian Ocean (Fig. 2C and Table S4). In general, the observed nitracline shoaling and phosphacline deepening are much stronger in southern (median $T_{NO_3} = -0.27 \text{ m yr}^{-1}$, $CI_{95\%} = [-0.40, -0.09]$; median $T_{PO_4} = 0.60 \text{ m yr}^{-1}$, $CI_{95\%} = [0.41, 0.71]$) compared to northern basins (median $T_{NO_3} = -0.02 \text{ m yr}^{-1}$, $CI_{95\%} = [-0.16, 0.13]$; median $T_{PO_4} = 0.13 \text{ m yr}^{-1}$, $CI_{95\%} = [-0.03, 0.35]$) (Table S4). Thus, the decline in phosphate-to-nitrate availability is most pronounced in the southern hemisphere.

10

15

20

Possible biogeochemical mechanisms for the observed trends

There are multiple possible biogeochemical drivers for shifting nutricline depths, including changes in phytoplankton resource demands, external nutrient inputs (riverine or atmospheric), or biological nitrogen fixation. First, it is commonly proposed that phytoplankton have an increasing N:P demand in a warming ocean due to a reduction of P-rich ribosomes needed for protein

synthesis (25). We find that this biochemical mechanism is unlikely to explain our results as it implies a faster deepening of the nitracline relative to the phosphacline. Second, changes in riverine inputs (26) and atmospheric deposition (27) of predominantly nitrogenous material can increase the demand for phosphorus relative to nitrogen. This mechanism is also unlikely to explain our results, as increasing nitrogenous input is primarily occurring in the northern hemisphere (26, 27), whereas a deepening phosphacline is mostly observed in the southern hemisphere (Fig. 2C and Table S4). Hence, neither changes in phytoplankton demands nor external inputs can explain the observed nutricline trends.

A third possibility is that changes in biological nitrogen fixation compensate for a declining supply of nitrate from stratification, but not for phosphate (22). Marine nitrogen fixation is often limited by iron (28 – 30), and for many reasons, this iron stress may be decreasing (31). Jiang et al. (2018) found that *Trichodesmium* cells use iron more efficiently at elevated temperature (32). Moreover, increasing stratification results in an increase in the Fe:N supply ratio by moderating the relative importance of vertical vs. aeolian nutrient supply (33). Deposition of soluble iron from combustion sources, including wildfire and fossil fuel burning, has been increasing in recent decades (34), and significantly impacting marine biogeochemistry (35). Considering these findings, diazotrophs are more commonly limited by iron in the southern and phosphorus in the northern hemisphere (36). Decreasing iron stress would therefore mostly stimulate nitrogen fixation and phosphate drawdown in the southern hemisphere. Hence, we hypothesize that the regulation of nitrogen fixation is important for the observed decline in phosphate-to-nitrate availability and can explain the hemispherical difference in depth trends.

Nutricline trends relate with ocean nitrogen fixation and stratification in CMIP6

To test this hypothesis, we compared trends in nitracline and phosphacline depths in the CMIP6 Earth System Models across historical and future emission scenarios (i.e., less and more stratified scenarios, respectively) (Fig. 3A-C). In the historical scenario, all models predicted nutricline trends notably smaller than the observed trends. In some models, equivalent trends for the nitracline and phosphacline depths at Redfield proportions (i.e., $T_{PO_4} = T_{NO_3}$) were seen. For other models, the phosphacline showed a faster deepening trend compared to the nitracline, whereas the opposite was never seen. These findings generally held true under future emission scenarios, although most models predicted faster deepening of both nitracline and phosphacline depths in the future. In conclusion, greater stratification generally led to a faster nutricline deepening in CMIP6, but some models included biogeochemical processes causing a faster deepening of the phosphacline relative to the nitracline.

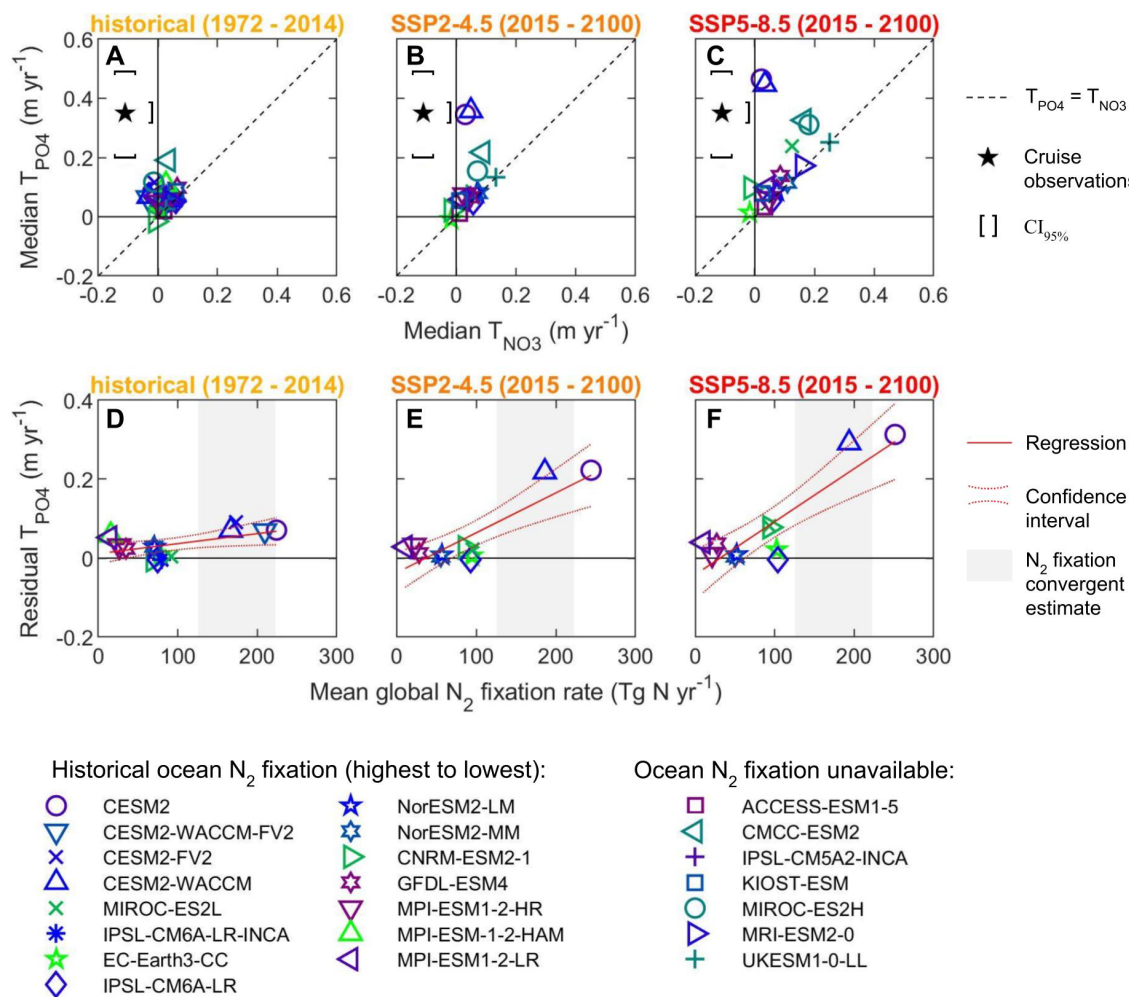


Figure 3: CMIP6 nutricline trends were linked to ocean nitrogen fixation. The first row shows CMIP6 predicted T_{NO3} and T_{PO4} under (A) historical, (B) middle-of-the-road (SSP2-4.5), and (C) business-as-usual (SSP5-8.5) emission scenarios (i.e., different stratification scenarios). (D-F) The second row is the relationship between declining phosphate-to-nitrate availability and ocean nitrogen fixation under each three scenarios. The decline of phosphate-to-nitrate availability was quantified as the residual T_{PO4} , which was the orthogonal distance from the $T_{PO4} = T_{NO3}$ line. The CMIP6 nitrogen fixation rates were global estimates averaged for the entire scenario time period. The convergent estimate of global ocean nitrogen fixation was quantified by Wang et al. (2019) using an inverse model and an Earth System Model (36).

The faster deepening of the phosphacline relative to the nitracline was correlated with ocean nitrogen fixation rates across Earth System Models (Fig. 3D-F). A differential deepening (i.e., residual T_{PO_4}) was quantified as the orthogonal distance from the $T_{PO_4} = T_{NO_3}$ line. Across all three model scenarios, we found significant positive relationships between ocean nitrogen fixation rates and the residual T_{PO_4} (Table S5). The correlation coefficients and regression slopes also increased with stronger emissions. This shows that the relationship between nitrogen fixation and declining phosphate-to-nitrate availability is dependent on the rate ocean warming and increasing stratification. Therefore, the CMIP6 model dynamics were consistent with the hypothesis that nitrogen fixation with stratification determines the faster deepening of the phosphacline relative to the nitracline.

Nutricline depths are influenced by nutrient uptake rates and iron deposition in CESM2

Among the CMIP6 models, CESM2 had the highest ocean nitrogen fixation rates as well as the highest residual T_{PO_4} . Although higher than most, this model was consistent with the convergent estimate of ocean nitrogen fixation quantified by Wang et al. (2019) (36). Finally, CESM2 showed nutricline trends that were the most consistent with observations. Hence, we next investigated different processes in CESM2 that may affect nitracline and phosphacline trends.

Flexible phytoplankton biomass composition may slow the deepening of the phosphacline relative to the nitracline. With a CESM2 model, Kwon et al. (2022) found that flexible rather than Redfield phosphate requirement led to reduced upper ocean phosphate demand by 2100 (37). We analyzed these same experiments and found that flexible phosphate uptake also led to shallower phosphacline depths (Fig. S8) (37). However, flexible phosphate uptake did not have a major effect

on nutricline trends through time (Fig. S8). Therefore, flexible nutrient uptake stoichiometry impacted the initial depths of nutriclines, but was not a factor for the long-term trends.

Decreasing iron stress may enhance the deepening of the phosphacline relative to the nitracline through stimulation of nitrogen fixation. (33, 34). In CESM2, we adjusted iron stress by increasing atmospheric iron deposition (D_{Fe}) rates either by hemisphere or globally (Fig. 4). Increased deposition rates increased nitrogen fixation and resulted in a faster deepening of the phosphacline relative to the nitracline (Fig. 4A,B). We again found a significant relationship between the residual T_{PO_4} and integrated nitrogen fixation (slope = $7 \times 10^{-4} \text{ m} \times [Tg N_{fix}]^{-1}$, slope SE = 2×10^{-4} m x $[Tg N_{fix}]^{-1}$, $p = 3 \times 10^{-3}$, $n = 10$). Additionally, we determined nutricline trends in regions with different primary nutrient limitations (Fig. 4C,D). Increased D_{Fe} led to a faster deepening of the phosphacline relative to the nitracline no matter the location, but the strongest effect was in iron-limited regions. This suggested that as iron stress was alleviated, it was eventually replaced with increased phosphorus stress. Thus, an increase in nitrogen fixation by alleviating iron stress directly results in a faster deepening of the phosphacline relative to the nitracline.

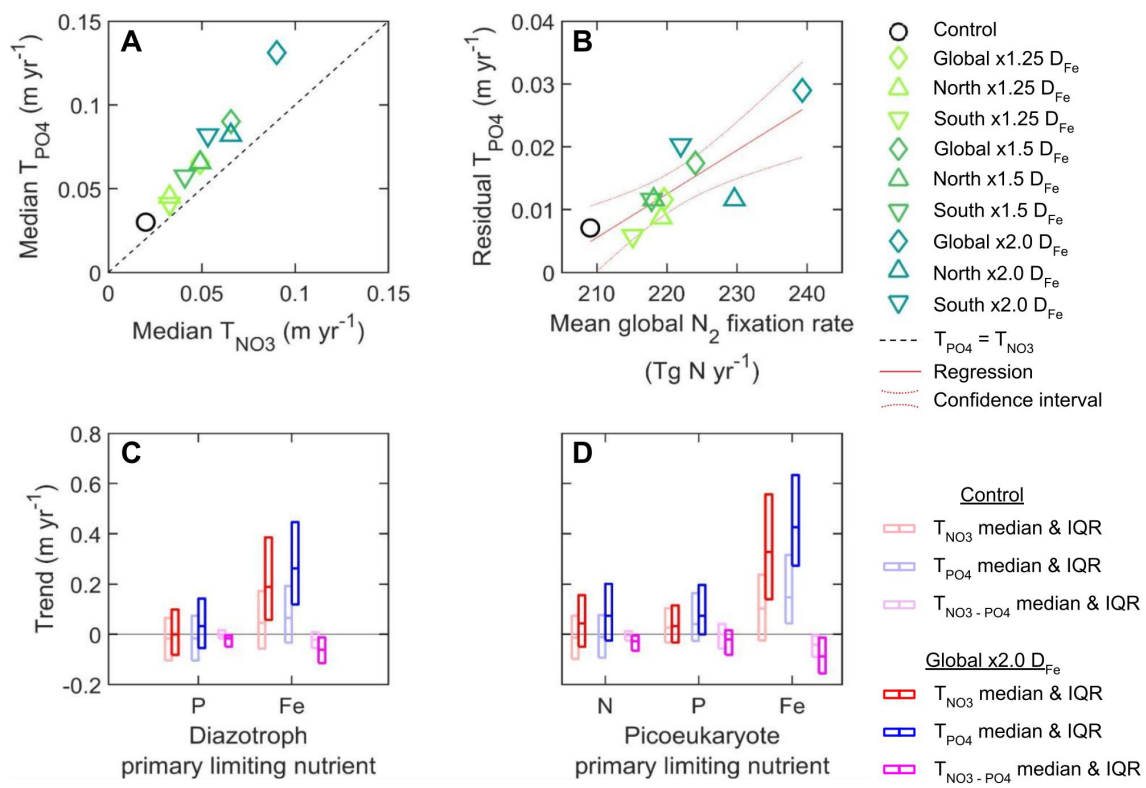


Figure 4: Increasing iron deposition in CESM2 augmented nitrogen fixation and phosphate-to-nitrate depletion. (A,B) The first row shows median nutricline trends from each iron deposition (D_{Fe}) experiment and the relationship between the residual T_{PO4} (i.e., the orthogonal distance from the $T_{PO4} = T_{NO3}$ line) and ocean nitrogen fixation rate. (C,D) The second row shows nutricline trends at sites grouped by primary nutrient limitation at the run's starting year. The center of each rectangle is the median trend, and the top and bottom edges are the 25th and 75th percentiles. $T_{NO3 - PO4}$ is the trend of $Z_{NO3} - Z_{PO4}$.

5

10

Caveats and conclusions

We presented evidence for a deepening of the phosphacline that is decoupled from any commensurate change in the nitracline. However, there are caveats to be considered. First, we restricted our global trend analysis to nutricline depths that were deeper than 50 m and from 45°S - 45°N. Omitting depths shallower than 50 m did not appreciably affect the observed trends, as they remained consistent when including depths deeper than 25 m (Tables S1 and S3). The applied

latitudinal range removed the Arctic Ocean from our analyses, despite this region experiencing some degree of nitrogen limitation (38). However, the sampling density in the Arctic was too low to quantify trends from nutricline depths that met our criteria. Furthermore, the Arctic experiences high variability in sea-ice cover, which is a major driver of stratification absent from the rest of the oligotrophic ocean (39). Second, there were notably less cruise observations from the earliest and latest years, but we still found a significantly faster deepening of the phosphacline from 1982 - 2012 (Tables S1 and S3). Third, ocean basins were sampled at different frequencies leading to less statistical power for some basins, most notably for the Indian Ocean. However, the nitrate and phosphate depth profiles were mostly sampled concurrently throughout time and space; thus, the sampling variability is not expected to have any effect on the differences in the trends observed for the two nutrients (Fig. S9). Fourth, although the global trends were robust, we recognize that variability in the phosphacline trends were more influenced by measurement error than the nutracline trends. Accounting for these caveats, we still find significant evidence for declining phosphate-to-nitrate availability over the past 5 decades (1972 - 2022).

The cruise observations suggest that phosphacline depths deepened by approximately 20 m over the past 5 decades, a rate that is almost an order of magnitude larger than most CMIP6 predictions for the historical period (Fig. 2-3, Tables S1 and S3). At the observed rate, nutrient availability throughout the southern oligotrophic gyres may soon resemble the western side of the North Pacific subtropical gyre (Fig. 1C and Table S2). This transition is possible due to the predicted decrease in iron stress for nitrogen fixation in this region (33, 34, 40). In turn, nutrient availability at the western side of the North Pacific subtropical gyre may soon resemble the North Atlantic subtropical gyre with widespread phosphorus stress (Fig. 1C and Table S2). A trend towards more phosphorus stress possibly driven by nitrogen fixation has already been observed in this area (41,

42). Therefore, the current patterns and trends in nutricline depths provide a basis for predicting which regions will begin to show increasing phosphorus stress for marine productivity.

Increasing phosphorus stress applies a selective pressure on marine phytoplankton, but some implications for ecosystems and elemental cycles remain uncertain. For instance, there is conflicting evidence whether total productivity should decline solely due to phosphorus limitation. Although phosphate has been suggested to be the ultimate control on phytoplankton production (1), variability in phytoplankton C:P and nitrogen fixation may buffer productivity despite increasing stratification (37, 43). In contrast, increasing nitrogen stress might have greater impacts on marine productivity, as phytoplankton have less ability to acclimate by modifying their C:N ratio (44). Nonetheless, phosphorus limitation does select for higher C:P in phytoplankton (45, 46), consequently reducing food quality throughout many marine food webs (47). These potential changes for marine ecosystems underscore the importance of constraining the rate of rising phosphorus stress throughout the ocean.

Increasing stratification and atmospheric iron inputs will likely continue in the coming decades (3, 31), but the decline in phosphate-to-nitrate availability is still subject to change. A declining phosphate supply would eventually start to limit nitrogen fixation rather than iron (48). Furthermore, continued deoxygenation from warming also increases denitrification, leading to greater declines in nitrate supplies (49). Therefore, the global trend toward phosphorus limitation could be temporary, but with an unknown duration. Continued efforts to monitor multiple nutrients and improve their model predictions should increase understanding of upper ocean biogeochemistry as the ocean continues to warm and stratify.

References and Notes:

1. Tyrrell, T. The relative influences of nitrogen and phosphorus on oceanic primary production. *Nature* **400**, 525–531 (1999).
2. Bopp, L., Monfray, P., Aumont, O., Dufresne, J.-L., Le Treut, H., Madec, G., Terray, L., & Orr, J. C. Potential impact of climate change on marine export production. *Global Biogeochemical Cycles* **15**, 81–99 (2001).
3. Fu, W., Randerson, J. T. & Moore, J. K. Climate change impacts on net primary production (NPP) and export production (EP) regulated by increasing stratification and phytoplankton community structure in the CMIP5 models. *Biogeosciences* **13**, 5151–5170 (2016).
4. Moore, J. K., Fu, W., Primeau, F., Britten, G. L., Lindsay, K., Long, M., Doney, S. C., Mahowald, N., Hoffman, F., & Randerson, J. T. Sustained climate warming drives declining marine biological productivity. *Science* **359**, 1139–1143 (2018).
5. Chassot, E., Bonhommeau, S., Dulvy, N. K., Mélin, F., Watson, R., Gascuel, D., & Le Pape, O. Global marine primary production constrains fisheries catches. *Ecology Letters* **13**, 495–505 (2010).
6. Schoepfer, S. D., Algeo, T. J., Ward, P. D., Williford, K. H. & Haggart, J. W. Testing the limits in a greenhouse ocean: Did low nitrogen availability limit marine productivity during the end-Triassic mass extinction? *Earth and Planetary Science Letters* **451**, 138–148 (2016).
7. Grasby, S. E., Knies, J., Beauchamp, B., Bond, D. P. G., Wignall, P., & Sun, Y. Global warming leads to Early Triassic nutrient stress across northern Pangea. *GSA Bulletin* **132**, 943–954 (2019).

8. Patey, M. D., Rijkenberg, M. J. A., Statham, P. J., Stinchcombe, M. C., Achterberg, E. P., & Mowlem, M. Determination of nitrate and phosphate in seawater at nanomolar concentrations. *TrAC Trends in Analytical Chemistry* **27**, 169–182 (2008).
9. Martiny, A. C., Lomas, M. W., Fu, W., Boyd, P. W., Chen, Y. L., Cutter, G. A., Ellwood, M. J., Furuya, K., Hashihama, F., Kanda, J., Karl, D. M., Kodama, T., Li, Q. P., Ma, J., Moutin, T., Woodward, E. M. S., & Moore, J. K. Biogeochemical controls of surface ocean phosphate. *Science Advances* **5**, eaax0341 (2019).
10. Sverdrup, H., Johnson, M. & Fleming, R, *The Oceans Their Physics, Chemistry, and General Biology* (New York: Prentice-Hall, Inc., 1942).
11. Letelier, R. M., Karl, D. M., Abbott, M. R. & Bidigare, R. R. Light driven seasonal patterns of chlorophyll and nitrate in the lower euphotic zone of the North Pacific Subtropical Gyre. *Limnology and Oceanography* **49**, 508–519 (2004).
12. Aksnes, D. L., Ohman, M. D. & Rivière, P. Optical effect on the nitracline in a coastal upwelling area. *Limnology and Oceanography* **52**, 1179–1187 (2007).
13. Richardson, K. & Bendtsen, J. Vertical distribution of phytoplankton and primary production in relation to nutricline depth in the open ocean. *Mar. Ecol. Prog. Ser.* **620**, 33–46 (2019).
14. Garcia, C. A., Baer, S. E., Garcia, N. S., Rauschenberg, S., Twining, B. S., Lomas, M. W. & Martiny, A. C. Nutrient supply controls particulate elemental concentrations and ratios in the low latitude eastern Indian Ocean. *Nature Communications* **9**, 4868 (2018).

15. Cermeño, P., Dutkiewicz, S., Harris, R. P., Follows, M., Schofield, O., & Falkowski, P. G. The role of nutricline depth in regulating the ocean carbon cycle. *Proceedings of the National Academy of Sciences* **105**, 20344–20349 (2008).
16. Herblard, A. & Voituriez, B. Hydrological structure analysis for estimating the primary production in the tropical Atlantic Ocean. *Journal of Marine Research* (1979).
17. Redfield, A. C. On the proportions of organic derivatives in sea water and their relation to the composition of plankton. *Liverpool: University Press of Liverpool* (1934).
18. Moore, C. M., Mills, M. M., Arrigo, K. R., Berman-Frank, I., Bopp, L., Boyd, P. W., Galbraith, E. D., Geider, R. J., Guieu, C., Jaccard, S. L., Jickells, T. D., La Roche, J., Lenton, T. M., Mahowald, N. M., Marañón, E., Marinov, I., Moore, J. K., Nakatsuka, T., Oschlies, A., Saito, M. A., Thingstad, T. F., Tsuda, A. & Ulloa, O. Processes and patterns of oceanic nutrient limitation. *Nature Geoscience* **6**, 701–710 (2013).
19. Browning, T. J. & Moore, C. M. Global analysis of ocean phytoplankton nutrient limitation reveals high prevalence of co-limitation. *Nature Communications* **14**, 5014 (2023).
20. Levitus, S., Conkright, M. E., Reid, J. L., Najjar, R. G. & Mantyla, A. Distribution of nitrate, phosphate and silicate in the world oceans. *Progress in Oceanography* **31**, 245–273 (1993).
21. Krom, M. D., Kress, N., Brenner, S. & Gordon, L. I. Phosphorus limitation of primary productivity in the eastern Mediterranean Sea. *Limnology and Oceanography* **36**, 424–432 (1991).
22. Wu, J., Sunda, W., Boyle, E. A. & Karl, D. M. Phosphate Depletion in the Western North Atlantic Ocean. *Science* **289**, 759–762 (2000).

23. Ustick, L. J., Larkin, A. A., Garcia, C. A., Garcia, N. S., Brock, M. L., Lee, J. A., Wiseman, N. A., Moore, J. K., & Martiny, A. C. Metagenomic analysis reveals global-scale patterns of ocean nutrient limitation. *Science* **372**, 287–291 (2021).
- 5
24. Messié, M. & Chavez, F. P. A global analysis of ENSO synchrony: The oceans' biological response to physical forcing. *Journal of Geophysical Research: Oceans* **117**, (2012).
25. Toseland, A., Daines, S. J., Clark, J. R., Kirkham, A., Strauss, J., Uhlig, C., Lenton, T. M., Valentin, K., Pearson, G. A., Moulton, V., & Mock, T. The impact of temperature on marine phytoplankton resource allocation and metabolism. *Nature Climate Change* **3**, 979–984 (2013).
- 10
26. Seitzinger, S. P. & Kroeze, C. Global distribution of nitrous oxide production and N inputs in freshwater and coastal marine ecosystems. *Global Biogeochemical Cycles* **12**, 93–113 (1998).
- 15
27. Mahowald, N. M., Scanza, R., Brahney, J., Goodale, C. L., Hess, P. G., Moore, J. K. & Neff, J. Aerosol Deposition Impacts on Land and Ocean Carbon Cycles. *Curr Clim Change Rep* **3**, 16–31 (2017).
28. Falkowski, P. G. Evolution of the nitrogen cycle and its influence on the biological sequestration of CO₂ in the ocean. *Nature* **387**, 272–275 (1997).
29. Michaels, A., Karl, D. & Capone, D. Element Stoichiometry, New Production and Nitrogen Fixation. *Oceanography* **14**, 68–77 (2001).

30. Moore, J. K., Doney, S. C., Lindsay, K., Mahowald, N. & Michaels, A. F. Nitrogen fixation amplifies the ocean biogeochemical response to decadal timescale variations in mineral dust deposition. *Tellus B* **58**, 560–572 (2006).
- 5 31. Hutchins, D. A. & Boyd, P. W. Marine phytoplankton and the changing ocean iron cycle. *Nature Climate Change* **6**, 1072–1079 (2016).
32. Jiang, H.-B., Fu, F.-X., Rivero-Calle, S., Levine, N. M., Sañudo-Wilhelmy, S. A., Qu, P.-P., Wang, X.-W., Pinedo-Gonzalez, P., Zhu, Z., & Hutchins, D. A. Ocean warming alleviates iron limitation of marine nitrogen fixation. *Nature Climate Change* **8**, 709–712 (2018).
- 10 33. Ward, B. A., Dutkiewicz, S., Moore, C. M. & Follows, M. J. Iron, phosphorus, and nitrogen supply ratios define the biogeography of nitrogen fixation. *Limnology and Oceanography* **58**, 2059–2075 (2013).
- 15 34. Hamilton, D. S., Moore, J. K., Arneth, A., Bond, T. C., Carslaw, K. S., Hantson, S., Ito, A., Kaplan, J. O., Lindsay, K., Nieradzik, L., Rathod, S. D., Scanza, R. A., & Mahowald, N. M. Impact of Changes to the Atmospheric Soluble Iron Deposition Flux on Ocean Biogeochemical Cycles in the Anthropocene. *Global Biogeochemical Cycles* **34**, e2019GB006448 (2020).
- 20 35. Wiseman, N. A., Moore, J. K., Twining, B. S., Hamilton, D. S. & Mahowald, N. M. Acclimation of Phytoplankton Fe:C Ratios Dampens the Biogeochemical Response to Varying Atmospheric Deposition of Soluble Iron. *Global Biogeochemical Cycles* **37**, e2022GB007491 (2023).

36. Wang, W.-L., Moore, J. K., Martiny, A. C. & Primeau, F. W. Convergent estimates of marine nitrogen fixation. *Nature* **566**, 205–211 (2019).
37. Kwon, E. Y., Sreeush, M. G., Timmermann, A., Karl, D. M., Church, M. J., Lee, S.-S. & Yamaguchi, R. Nutrient uptake plasticity in phytoplankton sustains future ocean net primary production. *Science Advances* **8**, eadd2475 (2022).
- 5
38. Ko, E., Gorbunov, M. Y., Jung, J., Joo, H. M., Lee, Y., Cho, K.-H., Yang, E. J., Kang, S.-H., & Park, J. Effects of Nitrogen Limitation on Phytoplankton Physiology in the Western Arctic Ocean in Summer. *Journal of Geophysical Research: Oceans* **125**, e2020JC016501 (2020).
- 10
39. Henley, S. F., Porter, M., Hobbs, L., Braun, J., Guillaume-Castel, R., Venables, E. J., Dumont, E., & Cottier, F. Nitrate supply and uptake in the Atlantic Arctic sea ice zone: seasonal cycle, mechanisms and drivers. *Philosophical Transactions of the Royal Society A: Mathematical, Physical and Engineering Sciences* **378**, 20190361 (2020).
- 15
40. Ellwood, M. J., Bowie, A. R., Baker, A., Gault-Ringold, M., Hassler, C., Law, C. S., Maher, W. A., Marriner, A., Nodder, S., Sander, S., Stevens, C., Townsend, A., van der Merwe, P., Woodward, E. M. S., Wuttig, K., & Boyd, P. W. Insights Into the Biogeochemical Cycling of Iron, Nitrate, and Phosphate Across a 5,300 km South Pacific Zonal Section (153°E–150°W). *Global Biogeochemical Cycles* **32**, 187–207 (2018).
- 20
41. Karl, D., Letelier, R., Tupas, L., Dore, J., Christian, J., & Hebel, D. The role of nitrogen fixation in biogeochemical cycling in the subtropical North Pacific Ocean. *Nature* **388**, 533–538 (1997).

42. Hashihama, F., Furuya, K., Kitajima, S., Takeda, S., Takemura, T., & Kanda, J. Macro-scale exhaustion of surface phosphate by dinitrogen fixation in the western North Pacific. *Geophysical Research Letters* **36**, (2009).
43. Bopp, L., Aumont, O., Kwiatkowski, L., Clerc, C., Dupont, L., Ethé, C., Gorgues, T., Séférian, R., & Tagliabue, A. Diazotrophy as a key driver of the response of marine net primary productivity to climate change. *Biogeosciences* **19**, 4267–4285 (2022).
44. Tanioka, T., Garcia, C. A., Larkin, A. A., Garcia, N. S., Fagan, A. J., & Martiny, A. C. Global patterns and predictors of C:N:P in marine ecosystems. *Communications Earth & Environment* **3**, 1–9 (2022).
45. Arrigo, K. R. Marine microorganisms and global nutrient cycles. *Nature* **437**, 349–355 (2005).
46. Galbraith, E. D. & Martiny, A. C. A simple nutrient-dependence mechanism for predicting the stoichiometry of marine ecosystems. *Proceedings of the National Academy of Sciences* **112**, 8199–8204 (2015).
47. Boersma, M., Aberle, N., Hantzsche, F. M., Schoo, K. L., Wiltshire, K. H., & Malzahn, A. M. Nutritional Limitation Travels up the Food Chain. *International Review of Hydrobiology* **93**, 479–488 (2008).
48. Sañudo-Wilhelmy, S. A., Kustka, A. B., Gobler, C. J., Hutchins, D. A., Yang, M., Lwiza, K., Burns, J., Capone, D. G., Raven, J. A., & Carpenter, E. J. Phosphorus limitation of nitrogen fixation by *Trichodesmium* in the central Atlantic Ocean. *Nature* **411**, 66–69 (2001).

49. Horak, R. E. A., Ruef, W., Ward, B. B. & Devol, A. H. Expansion of denitrification and anoxia in the eastern tropical North Pacific from 1972 to 2012. *Geophysical Research Letters* **43**, 5252–5260 (2016).
50. CCHDO Hydrographic Data Office (2023). CCHDO Hydrographic Data Archive, Version 2023-12-01. In CCHDO Hydrographic Data Archive. UC San Diego Library Digital Collections. <https://doi.org/10.6075/J0CCHKOT>.
51. Key, R. M., Olsen, A., Van Heuven, S., Lauvset, S. K., Velo, A., Lin, X., Schirnick, C., Kozyr, A., Tanhua, T., Hoppema, M., Jutterstrom, S., Steinfeldt, R., Jeansson, E., Ishii, M., Perez, F. F., & Suzuki, T (2015). Global Ocean Data Analysis Project, Version 2 (GLODAPv2), ORNL/CDIAC-162, ND-P093. Carbon Dioxide Information Analysis Center (CDIAC) https://doi.org/10.3334/CDIAC/OTG.NDP093_GLODAPV2.
52. Olsen, A., Key, R. M., van Heuven, S., Lauvset, S. K., Velo, A., Lin, X., Schirnick, C., Kozyr, A., Tanhua, T., Hoppema, M., Jutterström, S., Steinfeldt, R., Jeansson, E., Ishii, M., Pérez, F. F., & Suzuki, T. The Global Ocean Data Analysis Project version 2 (GLODAPv2) – an internally consistent data product for the world ocean. *Earth System Science Data* **8**, 297–323 (2016).
53. Boyer, T. P., Baranova, O. K., Coleman, C., Garcia, H. E., Grodsky, A., Locarnini, R. A., Mishonov, A. V., Paver, C. R., Reagan, J. R., Seidov, D., Smolyar, I. V., Weathers, K. & Zweng, M. M. (2018). World Ocean Database 2018. A.V. Mishonov, Technical Ed., NOAA Atlas NESDIS 87.
54. Fofonoff, N. P. & Millard, R. C. Calculation of Physical Properties of Seawater. UNESCO (1991).

55. Becker, S., Aoyama, M., Woodward, E. M. S., Bakker, K., Coverly, S., Mahaffey, C. & Tanhua, T. GO-SHIP Repeat Hydrography Nutrient Manual: The Precise and Accurate Determination of Dissolved Inorganic Nutrients in Seawater, Using Continuous Flow Analysis Methods. *Front. Mar. Sci.* **7**, 581790 (2020).
- 5 56. Gordon, L. I., Jennings, J. C., Ross, A. A. & Krest, J. M. A Suggested Protocol for Continuous Flow Automated Analysis of Seawater Nutrients (Phosphate, Nitrate, Nitrite and Silicic Acid) in the WOCE Hydrographic Program and the Joint Global Ocean Fluxes Study (1993).
- 10 57. Fofonoff, N. P. & Millard, R. C. Algorithms for the computation of fundamental properties of seawater. UNESCO (1983).
58. Leroy, C. C. & Parthiot, F. Depth-pressure relationships in the oceans and seas. *The Journal of the Acoustical Society of America* **103**, 1346–1352 (1998).
59. Kara, A. B., Rochford, P. A. & Hurlburt, H. E. Mixed layer depth variability over the global ocean. *Journal of Geophysical Research: Oceans* **108**, (2003).
- 15 60. Aoyama, M., Becker, S., Dai, M., Daimon, H., Gordon, L. I., Kasai, H., Kerouel, R., Kress, N., Masten, D., Murata, A., Nagai, N., Ogawa, H., Ota, H., Saito, H., Saito, K., Shimizu, T., Takano, H., Tsuda, A., Yokouchi, K. & Youenou, A. Recent Comparability of Oceanographic Nutrients Data: Results of a 2003 Intercomparison Exercise Using Reference Materials. *Analytical Sciences* **23**, 1151–1154 (2007).
- 20 61. Garcia, H. E., Boyer, T. P., Baranova, O. K., Locarnini, R. A., Mishonov, A. V., Grodsky, A., Paver, C. R., Weathers, K. W., Smolyar, I. V., Reagan, J. R., Seidov, D. & Zweng M. M. (2019). World Ocean Atlas 2018. NOAA National Centers for Environmental Information.

62. Lauvset, S. K., Key, R. M., Olsen, A., van Heuven, S., Velo, A., Lin, X., Schirnick, C.,
Kozyr, A., Tanhua, T., Hoppema, M., Jutterström, S., Steinfeldt, R., Jeansson, E., Ishii, M.,
Perez, F. F., Suzuki, T., & Watelet, S. A new global interior ocean mapped climatology: the
 $1^\circ \times 1^\circ$ GLODAP version 2. *Earth System Science Data* **8**, 325–340 (2016).
- 5 63. Séférian, R., Berthet, S., Yool, A., Palmiéri, J., Bopp, L., Tagliabue, A., Kwiatkowski, L.,
Aumont, O., Christian, J., Dunne, J., Gehlen, M., Ilyina, T., John, J. G., Li, H., Long, M. C.,
Luo, J. Y., Nakano, H., Romanou, A., Schwinger, J., Stock, C., Santana-Falcón, Y., Takano,
Y., Tjiputra, J., Tsujino, H., Watanabe, M., Wu, T., Wu, F. & Yamamoto, A. Tracking
Improvement in Simulated Marine Biogeochemistry Between CMIP5 and CMIP6. *Current
10 Climate Change Reports* **6**, 95–119 (2020).
64. O'Neill, B. C., Tebaldi, C., van Vuuren, D. P., Eyring, V., Friedlingstein, P., Hurtt, G.,
Knutti, R., Kriegler, E., Lamarque, J.-F., Lowe, J., Meehl, G. A., Moss, R., Riahi, K. &
Sanderson, B. M. The Scenario Model Intercomparison Project (ScenarioMIP) for CMIP6.
Geoscientific Model Development **9**, 3461–3482 (2016).
- 15 65. Meinshausen, M., Vogel, E., Nauels, A., Lorbacher, K., Meinshausen, N., Etheridge, D. M.,
Fraser, P. J., Montzka, S. A., Rayner, P. J., Trudinger, C. M., Krummel, P. B., Beyerle, U.,
Canadell, J. G., Daniel, J. S., Enting, I. G., Law, R. M., Lunder, C. R., O'Doherty, S., Prinn,
R. G., Reimann, S., Rubino, M., Velders, G. J. M., Vollmer, M. K., Wang, R. H. J. & Weiss,
R. Historical greenhouse gas concentrations for climate modelling (CMIP6). *Geoscientific
20 Model Development* **10**, 2057–2116 (2017).
66. Tsujino, H., Urakawa, S., Nakano, H., Small, R. J., Kim, W. M., Yeager, S. G.,
Danabasoglu, G., Suzuki, T., Bamber, J. L., Bentsen, M., Böning, C. W., Bozec, A.,

Chassagnet, E. P., Curchitser, E., Boeira Dias, F., Durack, P. J., Griffies, S. M., Harada, Y., Ilicak, M., Josey, S. A., Kobayashi, C., Kobayashi, S., Komuro, Y., Large, W. G., Le Sommer, J., Marsland, S. J., Masina, S., Scheinert, M., Tomita, H., Valdivieso, M. & Yamazaki, D. JRA-55 based surface dataset for driving ocean–sea-ice models (JRA55-do).
5 *Ocean Modelling* **130**, 79–139 (2018).

67. Long, M. C., Moore, J. K., Lindsay, K., Levy, M., Doney, S. C., Luo, J. Y., Krumhardt, K.

M., Letscher, R. T., Grover, M. & Sylvester, Z. T. Simulations With the Marine Biogeochemistry Library (MARBL). *Journal of Advances in Modeling Earth Systems* **13**, e2021MS002647 (2021).

10 68. Letscher, R. T., Moore, J. K., Martiny, A. C. & Lomas, M. W. Biodiversity and Stoichiometric Plasticity Increase Pico-Phytoplankton Contributions to Marine Net Primary Productivity and the Biological Pump. *Global Biogeochemical Cycles* **37**, e2023GB007756 (2023).

15 69. Huang, B., Thorne, P. W., Banzon, V. F., Boyer, T., Chepurin, G., Lawrimore, J. H., Menne, M. J., Smith, T. M., Vose, R. S. & Zhang, H.-M. (2017). NOAA Extended Reconstructed Sea Surface Temperature (ERSST), Version 5. NOAA National Centers for Environmental Information. <https://doi.org/10.7289/V5T72FNM>.

20 70. Webb, E. J. & Magi, B. I. The Ensemble Oceanic Niño Index. *International Journal of Climatology* **42**, 5321–5341 (2022).

Acknowledgments: We thank the many researchers who have collected hydrographic data and shared their results as part of this global analysis. We thank those involved in CCHDO, GLODAP,

and WOD for conglomerating and managing these cruise data sets. We thank Jennifer Martiny and François Primeau for their helpful suggestions on our initial manuscript. We thank Eun Young Kwon and Mohanan Sreeush for their assistance in providing their CESM2 nutrient uptake experiments. We acknowledge that we referred to ChatGPT 3.5 for suggesting code in data analysis and edits in the manuscript text.

Funding: For support, we thank the National Science Foundation (1559002, 1848576, and 5 1948842 to ACM), the National Oceanic and Atmospheric Administration (101813-Z7554214 to ACM), the National Aeronautics and Space Administration (80NSSC21K1654 to ACM), the Office of Biological and Environmental Research (BER) within the Department of Energy 10 (DOE) Earth System Model Development program (DE-SC0022177 to JKM), the DOE BER Regional and Global Model Analyses Program RUBISCO SFA (to JKM), and the National Science Foundation (OCE-2124014 to JKM).

Author contributions:

Conceptualization: ACM

Methodology: SDG, JY, JKM, ACM

Investigation: SDG

Funding acquisition: JKM, ACM

Project administration: ACM

Supervision: JKM, ACM

Writing – original draft: SDG, ACM

Writing – review & editing: SDG, JY, JKM, ACM

Competing interests: Authors declare that they have no competing interests.

Data and materials availability: Nutricline data from the cruise observations are provided as Data Set S1. This data and all of the essential code for analyzing the observations and models are deposited in Dryad (<https://doi.org/10.5061/dryad.v41ns1s4v>). Interpolated maps were created using Ocean Data View, and all statistical analyses were performed using MATLAB R2021b.

5

List of Supplementary Materials:

Materials and Methods

Figs. S1 to S9

Tables S1 to S6

References (50 – 70)

Supplementary Materials for

Observed declines in upper ocean phosphate-to-nitrate availability

Skylar D. Gerace¹, Jun Yu¹, J. Keith Moore¹, Adam C. Martiny^{1,2}

Corresponding author: amartiny@uci.edu

The PDF file includes:

Materials and Methods

Figs. S1 to S9

Tables S1 to S6

References (50 – 70)

Materials and Methods

Conglomerate cruise data sets

We quantified nutricline depths from 1,060 cruise data sets provided by the CLIVAR and Carbon Hydrographic Data Office (50). Each cruise data set was formatted in a standardized netCDF4 format following the Climate and Forecast (CF) Conventions version 1.8. These data sets included hydrographic data measured mostly as part of the Global Ocean Ship-Based Hydrographic Investigations Program (GO-SHIP). Other precursor programs of repeat hydrography, such as the World Ocean Circulation Experiment (WOCE), were included as well. We refer to the conglomerate data set from CCHDO as the GO-SHIP data set throughout the main manuscript.

We also compared our results from GO-SHIP with results from two other conglomerate data sets. We defined nutricline depths from 1,086 cruise data sets provided by the Global Ocean Data Analysis Project merged and adjusted data product (GLODAPv2.2022) (51, 52). Nutrient concentrations in GLODAPv2.2022 were adjusted to account for measurement biases with time (51, 52). Therefore, GLODAPv2.2022 may have revealed potential measurement biases in the GO-SHIP data set. We also referred to nutrient concentrations found in the World Ocean Database (WOD) (53). Although WOD did not prioritize repeat hydrography, this database held 12,707 unique cruise data sets from 1972 to 2022. Despite having the least amount of cruise data sets, we chose to focus our analysis on the GO-SHIP data set since its purpose is to provide quality-controlled measurements of repeat hydrography.

Cruise sampling methods

On the GO-SHIP cruises, temperature and salinity were recorded at various depths and stations using a Conductivity Temperature Depth (CTD) instrument (54). Nutrients were sampled from seawater collected by a Niskin bottle rosette fitted onto the CTD (55). Nutrient concentrations were photometrically determined from the collected seawater via continuous flow analysis. Nitrate was determined by first reducing nitrate to nitrite in a copperized cadmium column. A sulfanilamide solution and N-Naphthylethylene-diamine were introduced to produce a red azo dye (55, 56). To determine phosphate, molybdic acid was introduced to form phosphomolybdic acid. The phosphomolybdic acid was reduced to phosphomolybdate acid with hydrazine to produce a blue solution (55, 56).

Nutrient concentrations

Here, we analyzed each CTD cast where nitrate or phosphate was measured. Nitrate profiles inclusive of nitrite concentrations (i.e., nitrate + nitrite) were excluded from our analysis, as were any negative or outlier concentrations. We defined outlier concentrations as instances where a nutrient decreased with depth by more than $10 \text{ } \mu\text{mol kg}^{-1}$ in the upper ocean. Nutrient concentrations were predominantly in units of $\mu\text{mol kg}^{-1}$, but for concentrations expressed as $\mu\text{mol L}^{-1}$, we converted them to $\mu\text{mol kg}^{-1}$ by calculating seawater density. We calculated density using a UNESCO formula by incorporating temperature ($^{\circ}\text{C}$) and salinity (psu) measurements included in each bottle file (57).

Interpolating nutrients with pressure

For every cast with nutrient measurements at 2 or more pressures, we linearly interpolated nitrate and phosphate concentrations for every 1 dbar down to a maximum pressure of 1000 dbar. The interpolation only spanned between the lowest and highest pressures with nutrient measurements. Similarly, we interpolated temperature and salinity from the respective cruise CTD file for every 1 dbar. We then recorded the nutricline as the pressure and density where the interpolated nutrient concentrations first reached threshold concentrations. The nutricline pressure was converted to depth (m) using a UNESCO formula revised by Leroy & Parthiot (1998) (58).

Nutricline concentration thresholds

Our analysis focused on nutricline depths defined by a threshold concentration of $3 \mu\text{mol kg}^{-1}$ for nitrate and the Redfield (1934) proportion equivalent for phosphate (i.e., $3/16 \mu\text{mol kg}^{-1}$, assuming that N:P = 16:1) (17). We chose these threshold concentrations that were higher than other studies (13 - 15) to minimize influence from surface mixing and ensure detectability of low phosphate concentrations (8, 9). We also quantified nutricline trends in the GO-SHIP data set using lower ($[\text{NO}_3^-] = 1 \mu\text{mol kg}^{-1}$ and $[\text{PO}_4^{3-}] = 1/16 \mu\text{mol kg}^{-1}$) and higher ($[\text{NO}_3^-] = 5 \mu\text{mol kg}^{-1}$ and $[\text{PO}_4^{3-}] = 5/16 \mu\text{mol kg}^{-1}$) threshold concentrations. This determined if the chosen threshold concentrations had a considerable effect on the nutricline trends.

Criteria for nutricline depths

We followed a series of criteria for quantifying nutricline depths and trends to improve the accuracy of our analyses. First, we only recorded the nutricline depth of a cast if there existed interpolated concentrations above and below said depth. Second, we binned the coordinates of

each nutricline depth to the nearest degree of latitude and longitude to quantify average nutricline depths per unique coordinate and year. Lastly, we quantified trends only from average nutricline depths that were deeper than 50 m and at a latitude from 45°S to 45°N. We also repeated our analysis using a depth boundary of 25 m. We selected these boundaries to target trends in regions where nutrients limit growth, and minimize effects from seasonal changes in stratification (59). We address potential biases resulting from these spatial boundaries in the “Caveats and conclusions” section.

Significance tests for nutricline trends

We tested the significance of nutricline trends using two independent methods. First, we fitted linear regression models to average nutricline depths through time. These nutricline depths were annual averages for each unique geographic coordinate. Two separate regressions were fitted to nitracline and phosphaclines, and an *F*-test determined if each regression was significant (i.e., $p < 0.05$). Second, we analyzed each geographic coordinate that had average nutricline depths recorded for two or more unique years. For each coordinate, we fitted a regression to its average nutricline depths vs. years to quantify its site-specific trend. These site-specific trends were quantified separately for nitraclines and phosphaclines. The sign test determined if the global median site-specific trend was significantly different from zero. Additionally, the Kruskal-Wallis test determined if the median trends of nitracline and phosphaclines were significantly different from each other. We also calculated 95% confidence intervals (CI_{95%}) for the median trends by generating 10,000 bootstrap samples of the data set. Thus, with global regressions and site-specific trends, we were able to test if nitracline and phosphacline depths were generally shifting in recent decades.

Comparing trends from random populations

In addition to the significance tests, we randomized sampling time of the nutriclines to further examine the robustness of the observed trends. We constructed 10,000 randomized conglomerate data sets by scrambling the years of nutricline depths, where each depth was an annual-average for a unique geographic coordinate. For each of these 10,000 random populations, we found the median values of the site-specific trends for nutricline depths. We recorded these median trends of random populations (MToRP) and determined the portion of MToRP with an absolute value higher than the absolute value of the observed median trend. Quantifying this portion of the MToRP distribution served as a two-tailed *p* value to test the significance of the observed median trend.

We also investigated how measurement error may have affected the nutricline trends. From an intercomparison study of nutrient detection, nitrate and phosphate concentrations had average standard deviations of about 400 nmol kg⁻¹ and 50 nmol kg⁻¹ respectively (60). We added additional error to the GO-SHIP observations by creating two normal distributions of values. Both distributions had means equal to zero, and standard deviations equal to twice the values from Aoyama et al. (2007) (i.e., 800 nmol kg⁻¹ and 100 nmol kg⁻¹) (60). For every nutrient concentration in the observations, we randomly sampled a value from either the first or second distribution depending on whether the nutrient was nitrate or phosphate. We added this sampled value to the nutrient concentration to impose additional measurement error. We then quantified nutricline depths and trends after altering all concentrations. We then compared the median values and variability of the site-specific trends to those from the unaltered observations.

Investigating biases with climatologies

To explore potential temporal biases in the cruise observations, we analyzed nutrient concentrations from the National Oceanic and Atmospheric Administration's World Ocean Atlas data product version 2018 (WOA18). WOA18 is an objectively-analyzed global climatology of nutrient concentrations per 1° of latitude and longitude for every month (61). The vertical profiles reached down to 800 m deep with depth bin sizes ranging 5 - 50 m. For every geographic coordinate, we interpolated nitrate and phosphate concentrations per 1 m and found the average nutricline depths.

We investigated WOA18 to reveal if there was a notable bias in the months nutriclines were sampled. First, we indexed each nutricline depth based on the latitude, longitude, and month of the respective cast. We then replaced each observed nutricline depth with its respective monthly value in WOA18. Next, we proceeded to find the annually-averaged nutricline depth for each geographic coordinate of each year. Then, we determined the trends of nutricline depths with time. If there were considerable seasonal biases in cruise casts, then the global medians of these trends would deviate from zero.

We also constructed random populations from WOA18 to determine how variability in site-specific trends affected their median values. First, we randomly selected a potential monthly nutricline depth for each geographic coordinate with nutricline depths observed for two or more years in the GO-SHIP collection. We then paired these to another random, potential monthly nutricline depth to simulate a 50-year trend for each geographical coordinate. We repeated this procedure until 10,000 random populations of the conglomerate data set were made. Second, we

performed a similar procedure where we paired one set of monthly values to another set, but here we imposed a ubiquitous site-specific trend by changing the second set of monthly values by a rate equivalent to the median trend from observations. These two analyses determined if the median trend was controlled by monthly variability in sampling. Third, we imposed a variable site-specific trend by changing each monthly value in the second set by a rate of change randomly selected from a normal distribution of rates. We altered the mean and standard deviation of this normal distribution until the median trend and the variance of simulated nutricline depths (i.e., IQR) both matched the observations. This analysis determined if the median trend actually captured an underlying tendency of the site-specific trends despite their high variability. In summary, these analyses with WOA18 determined if variability in the site-specific trends had considerable influence on their median values.

Improved technology may have increased the accuracy of nutrient concentrations over time. To test this, we investigated GLODAPv2.2016, another mapped climatology of nutrient concentrations for each 1° of latitude and longitude (51, 62). GLODAPv2.2016 provided nitrate and phosphate concentrations down to 5,500 m with depth bins ranging from 10 - 500 m. At each geographical coordinate, we linearly interpolated nutrient concentrations for every 1 m of depth. We then recorded the interpolated concentrations at the depths of 100, 300, 500, 1,000, 2,000, 3,000, and 4,000 m for each coordinate. Next, we went through each cast of the GO-SHIP observations and recorded the interpolated concentrations at these same depths. For each cast, we found the difference of the observed concentrations and the mapped climatology at these specified depths. We then fitted linear regressions to the differences at each coordinate. If improved

technology imposed a measurement bias, then the differences at deeper depths may show a negative trend with time.

CMIP6 predicted nutriclines

The Coupled Model Intercomparison Project Phase 6 (CMIP6) is a collection of global models that each predict biogeochemical cycles with time (63). Séférian et al. (2020) outline some key model differences that contribute to their contrasting predictions of biogeochemistry. These models differ in their ocean-climate interactions, organic matter cycling rates, marine plankton communities, biological processes, nutrient ratios, and more (63).

Here, we analyzed nutrient concentrations from CMIP6 under three emission scenarios: the historical period, middle-of-the-road (SSP2-4.5), and business-as-usual (SSP5-8.5) (Table S6) (64, 65). For the historical scenario, we confined the years to 1972 - 2014 to better match the time span of the observations. The future emission scenarios were confined to the years 2015 - 2100. Our primary variables of interest were marine concentrations of nitrate and phosphate (“no3” and “po4” respectively). We also analyzed sea temperature (“thetao”) and salinity (“so”) through time to convert the nutrient concentrations from mol m⁻³ to µmol kg⁻¹, and determine trends in nutricline densities. These variables came from consistent model variants in terms of realization, initialization, method, physics, and forcing; the “r1i1p1f1” variant was used when available. With these variables, we quantified nitracline and phosphacline depths with time.

Nutricline depths in CMIP6 were quantified similar to the cruise observations. For each model grid point, we linearly interpolated nutrient concentrations for every 1 dbar of pressure up to 1000

dbar. Pressure was converted to meters of depth using a UNESCO formula revised by Leroy & Parthiot (1998) (58). Model grid points were then rounded to the nearest degree of latitude and longitude to quantify average nutricline depths and densities for each unique geographical coordinate and year. We analyzed trends from each coordinate within 45°S - 45°N that had average nutricline depths deeper than 50 m for two or more unique years. Lastly, we tested if trends in vertically-integrated ocean nitrogen fixation rates (“intpn2”) were related to predicted nutricline trends. Accordingly, we determined if CMIP6 was consistent with our hypothesis that nitrogen fixation rates together with stratification drive the decline of phosphate-to-nitrate availability.

CESM2 phosphate uptake and D_{Fe} experiments

We explored two potential drivers of nutricline trends in the Community Earth System Model version 2 (CESM2). First, we tested if flexible C:P in phytoplankton affected nutricline trends, which essentially tested if flexible phosphate uptake rates had any effect. We analyzed two experimental scenarios from Kwon et al. (2022), one where phytoplankton C:P is fixed at Redfield proportions (16:1), and another where phytoplankton C:P increased with declining phosphate concentrations as a power-law function (37). These experiments were conducted under historical and SSP3-7.0 emission scenarios. For these experiments, we quantified nutricline depths using the same method as the CMIP6 models, with the exception that nutrient concentrations were left in units of mmol m⁻³. Therefore, the nitracline and phosphacline were defined based on 3 mmol m⁻³ and 3/16 mmol m⁻³, respectively.

The second potential driver we tested is iron deposition (D_{Fe}) in CESM2. To begin this analysis, we initialized the simulation with JRA55-do (66) interannual temperature forcing (1958-2018, 61

years) for five repeated cycles (305 years in total), using a modified version of the CESM2-MARBL ecosystem (67). We ran a control run after the 305-year initialization, where historical emissions continued for another 61 years. For experimental runs, we tested how nitrogen fixation rates and nutricline depths responded to changing D_{Fe} either increasing globally, in just the northern hemisphere, or in just the southern hemisphere. We augmented D_{Fe} in these areas by either 25%, 50%, or 100%. Each experimental run started immediately after the 305-year initialization and lasted for 61 years as well. Therefore, a total of 9 experimental runs were conducted to constrain how D_{Fe} affects nitrogen fixation rates and nutricline trends in CESM2. For this analysis, nutrient concentrations were converted to $\mu\text{mol kg}^{-1}$ and nutricline depths were quantified using the same method as the CMIP6 models.

CESM2-MARBL encompasses many essential features of marine ecosystems, including major limiting macronutrients (N, P, Si), iron cycling processes, variable nutrient assimilation ratios, mineral ballasting, a Q10 growth parameterization, and dynamic dissolved organic matter (DOM) cycling (67). While the standard version of MARBL has three phytoplankton types (small phytoplankton, diazotrophs and diatoms) and one zooplankton, we used an updated version of MARBL in this study which includes eight types of phytoplankton and four types of zooplankton (MARBL-8P4Z) (Yu et al., *in prep*). For phytoplankton, the 8P4Z model includes 1) pico-sized phytoplankton (0.5-2.0 μm): *Prochlorococcus*, *Synechococcus*, pico-eukaryotes and nitrogen-fixing diazotrophs; 2) nano-sized phytoplankton: *Phaeocystis* (2-10 μm), coccolithophores (5-10 μm) and generic other nanophytoplankton (2-200 μm); 3) micro-sized phytoplankton (20-200 μm): diatoms. For zooplankton, the 8P4Z model includes small microzooplankton (5-20 μm , ciliates, nanoflagellates), large microzooplankton (20-200 μm ,

copepod nauplii, small dinoflagellates etc.), mesozooplankton (200-2000 µm, smaller copepod, large dinoflagellates) and macrozooplankton (>2000 µm, larger copepod, krill). Besides the modified plankton types, the 8P4Z model also has a better representation of the phytoplankton group-specific variable stoichiometries, both for iron (35) and for the macronutrients (N, P, Si) (68).

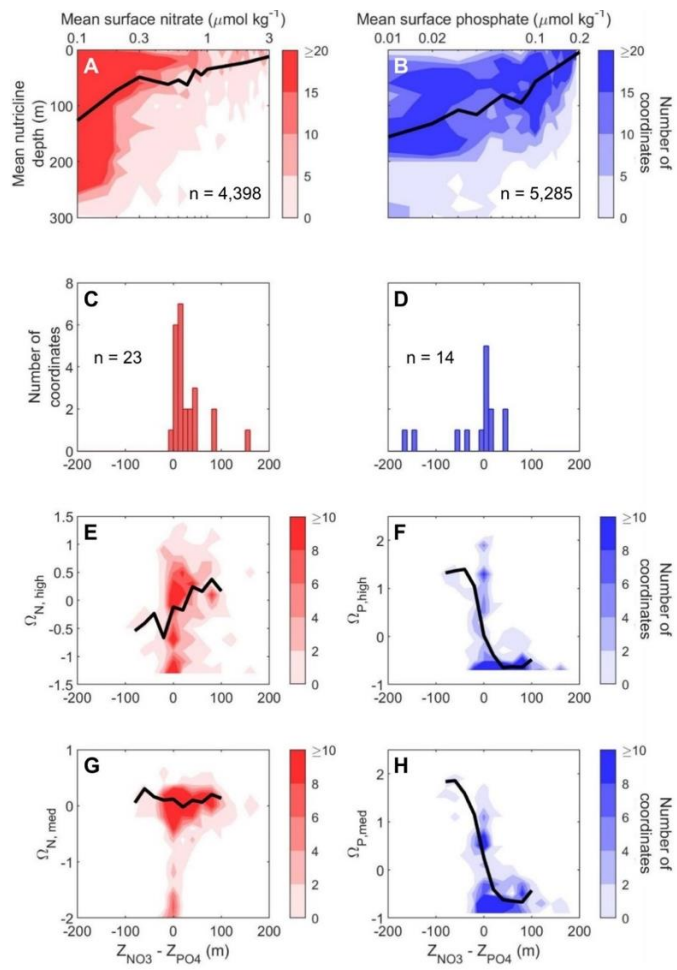


Figure S1: Nutricline depths were linked to upper ocean nutrient availability and limitation. The first row shows mean values (1972 - 2022) of (A) nitracline and (B) phosphacline depths vs. mean values of surface nutrient concentrations for each geographic coordinate (n). Nutricline depths were determined from GO-SHIP using threshold concentrations of $[NO_3^-] = 3 \mu\text{mol kg}^{-1}$ and $[PO_4^{3-}] = 3/16 \mu\text{mol kg}^{-1}$. The black lines are moving medians with bins that were logarithmically-spaced from 10^{-2} to 10^1 . The second row shows mean values of $Z_{NO_3} - Z_{PO_4}$ for each geographic coordinate where there was (C) nitrogen limitation without phosphorus limitation, and (D) phosphorus limitation determined by bioassay experiments conglomerated by Browning & Moore (2023) (19). The third and fourth rows are mean values of $Z_{NO_3} - Z_{PO_4}$ for each geographic coordinate ($n = 353$) where there was (E) high nitrogen stress, (F) high phosphorus stress, (G) medium nitrogen stress, and (H) medium phosphorus stress determined by *Prochlorococcus* genetic biomarkers in Ustick et al. (2021) (23). The black lines are moving medians with bins spaced every 10 m.

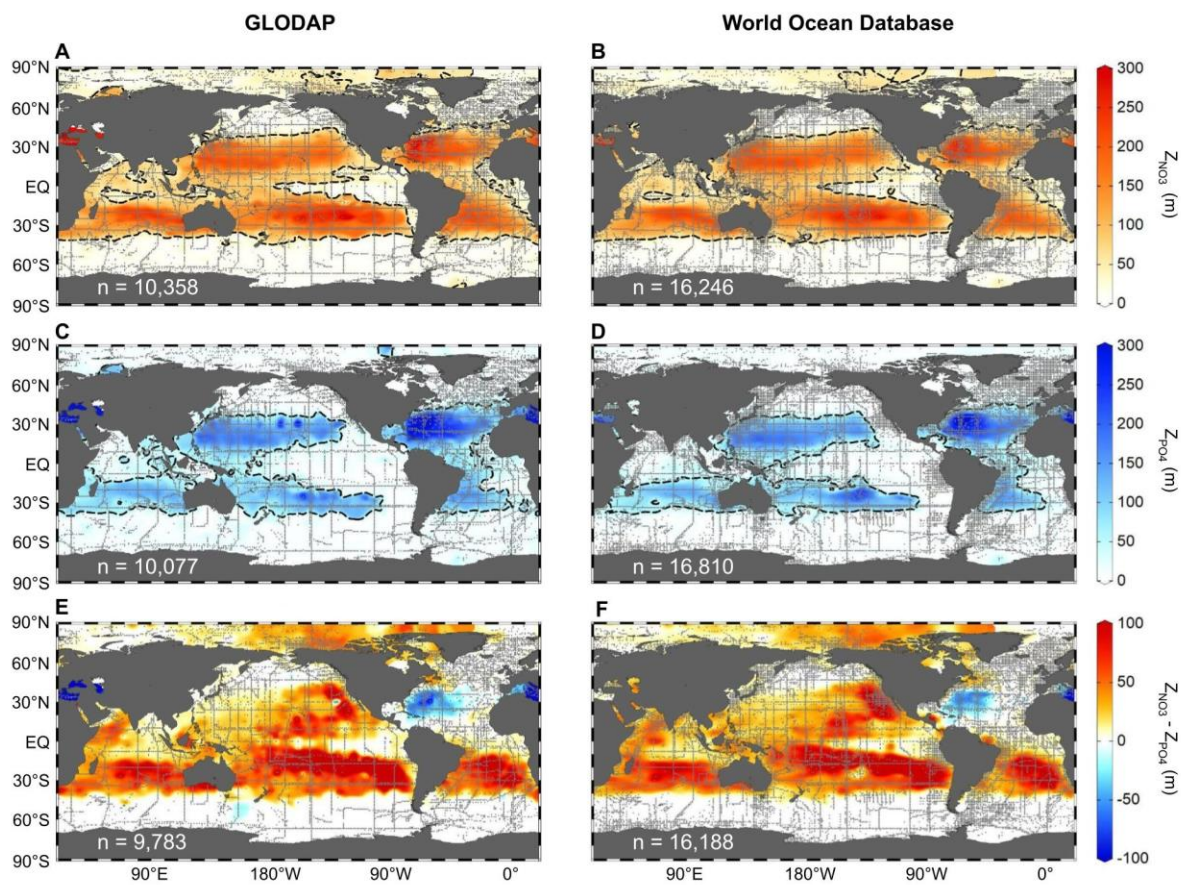


Figure S2: Mean nutricline depths from other conglomerate data sets were consistent with GO-SHIP. (A,B)

Average nitracline depths (Z_{NO_3}), (C,D) average phosphacline depths (Z_{PO_4}), and (E,F) the difference of average nitracline and phosphacline depths ($Z_{NO_3} - Z_{PO_4}$) from the GLODAPv2.2022 merged and adjusted data product and the World Ocean Database (WOD), respectively. Z_{NO_3} and Z_{PO_4} were defined with threshold concentrations of $[NO_3^-] = 3 \mu\text{mol kg}^{-1}$ and $[PO_4^{3-}] = 3/16 \mu\text{mol kg}^{-1}$, respectively. Here, Z_{NO_3} and Z_{PO_4} were averaged from 1972 to 2022 for each unique geographic coordinate (gray dots with sample size “n”). The dashed line is the contour at 50 m depth. The depth differences were calculated using the averaged depths.

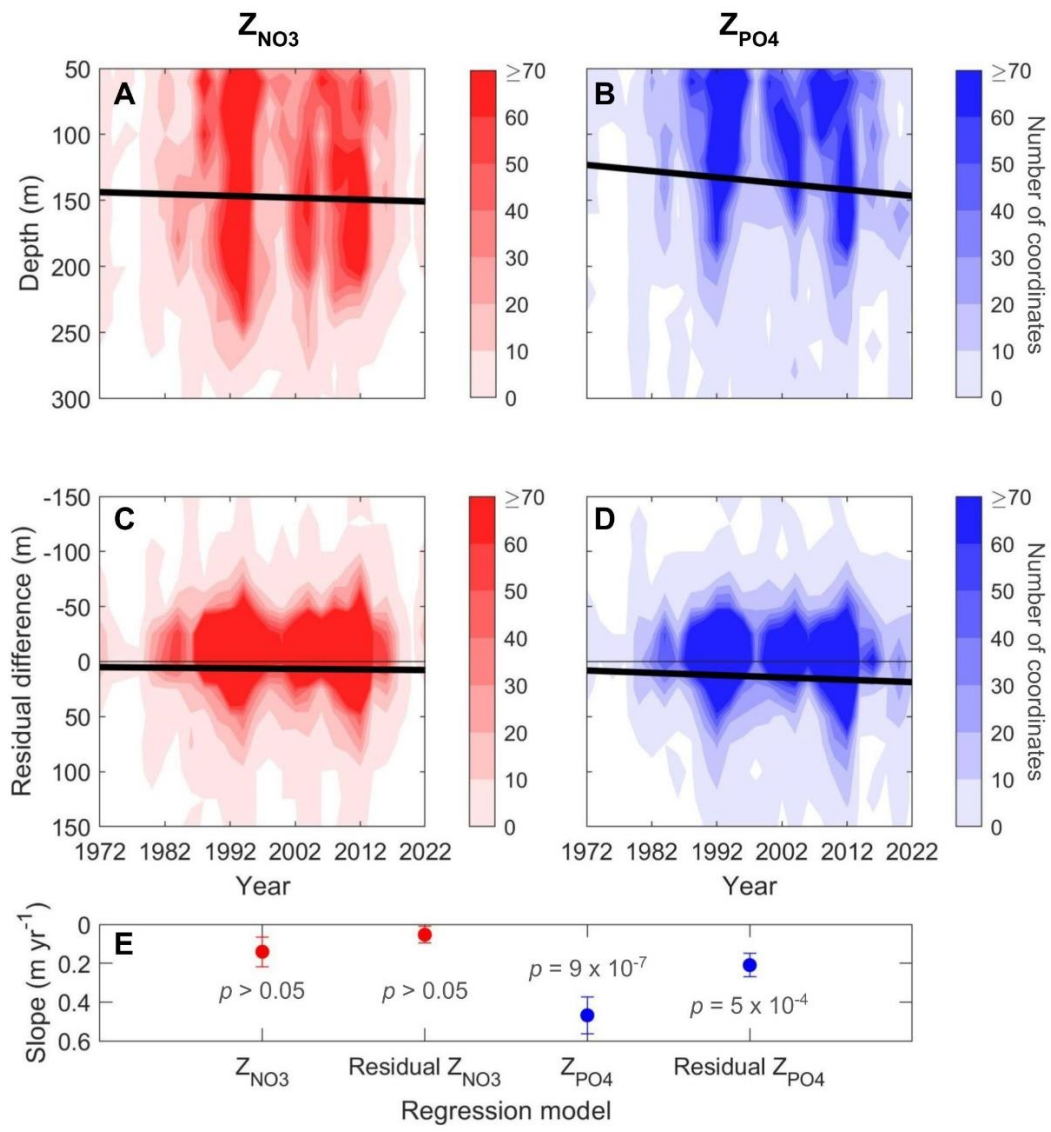


Figure S3: Global regressions show a faster deepening of Z_{PO_4} relative to Z_{NO_3} . Here, Z_{NO_3} and Z_{PO_4} were average values from the GO-SHIP data set for each unique geographic coordinate and year. They were defined with threshold concentrations of $[\text{NO}_3^-] = 3 \mu\text{mol kg}^{-1}$ and $[\text{PO}_4^{3-}] = 3/16 \mu\text{mol kg}^{-1}$. Linear regressions fitted to (A) Z_{NO_3} with time ($n = 7,513$) and (B) Z_{PO_4} with time ($n = 6,823$). We also subtracted the WOA18 monthly nutricline depths from observations to fit linear regressions to the residual differences of (C) Z_{NO_3} ($n = 7,680$) and (D) Z_{PO_4} ($n = 6,365$) with time. (E) The slopes of each regression model with their respective p values. The error bars are their standard errors.

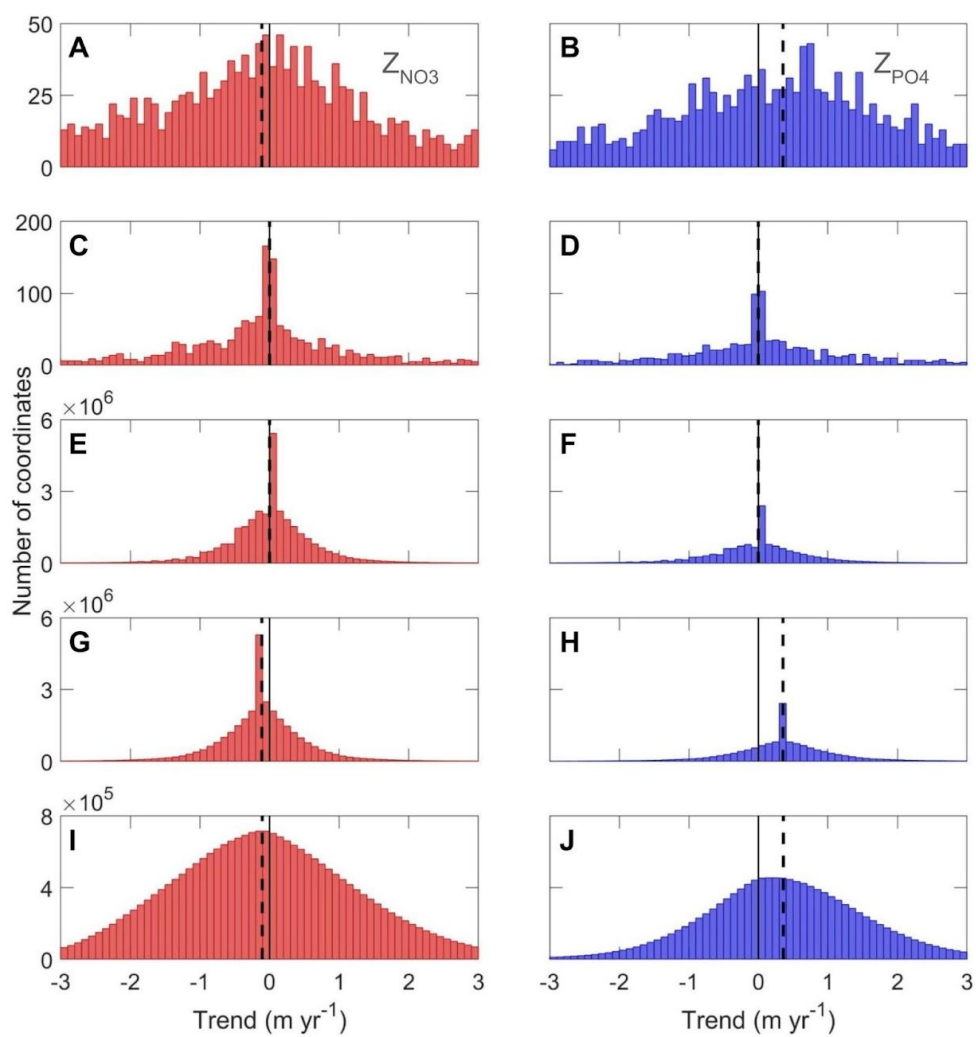


Figure S4: World Ocean Atlas shows that the median trends capture the underlying tendency of site-specific trends. (A,B) Observed site-specific trends of nitracline and phosphacline depths from GO-SHIP. (C,D) Site-specific trends after substituting GO-SHIP observations with their respective monthly values in World Ocean Atlas version 2018 (WOA18). (E,F) Simulated site-specific trends of 10,000 random populations of paired WOA18 monthly values. (G,H) Simulated site-specific trends of 10,000 random populations after imposing a ubiquitous trend on WOA18 monthly values. The ubiquitous trend was equivalent to the observed median trend from GO-SHIP. (I,J) Simulated site-specific trends of 10,000 random populations after imposing a variable site-specific trend on WOA18 monthly values. Each site-specific trend came from a normal distribution with a mean and standard deviation selected such that the median trend and variance in depths were the same as the GO-SHIP observations. The dashed lines mark the median values.

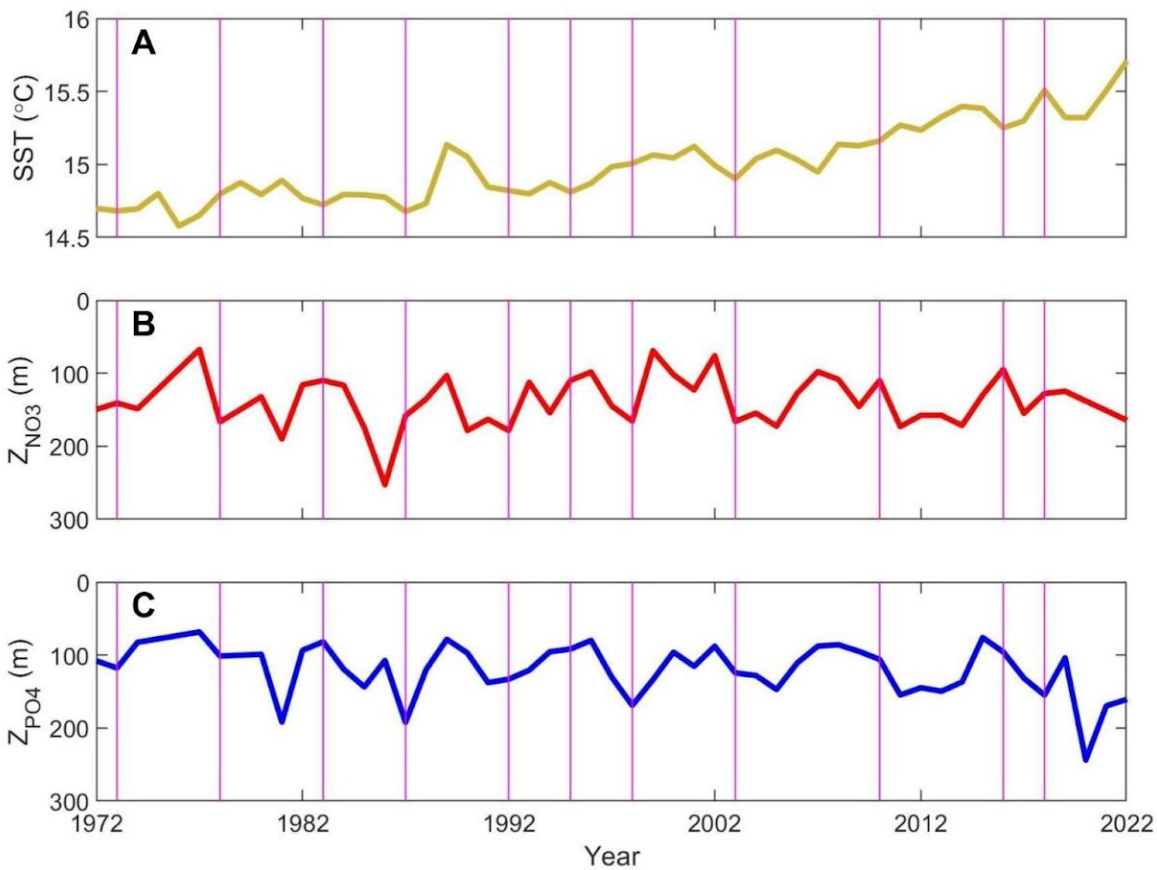


Figure S5: The ENSO cycle and other climate phenomena may affect interannual nutricline variance. Annual median values of (A) sea surface temperature (69), (B) nitracline depth, and (C) phosphacline depth. Nutricline depths were quantified from the GO-SHIP data set using threshold concentrations of $[NO_3^-] = 3 \mu\text{mol kg}^{-1}$ and $[PO_4^{3-}] = 3/16 \mu\text{mol kg}^{-1}$. The magenta lines denote El Niño years determined by the Ensemble Oceanic Niño Index (70).

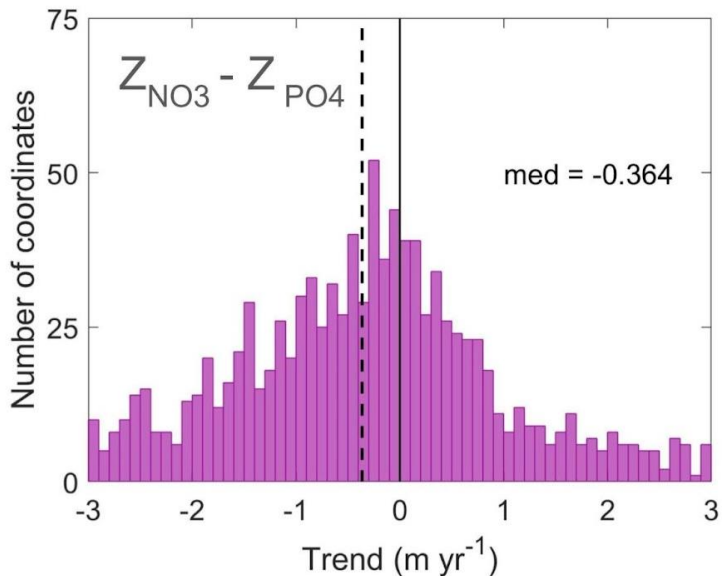


Figure S6: The median trend of $Z_{\text{NO}_3} - Z_{\text{PO}_4}$ was negative, suggesting Z_{PO_4 deepened faster. Z_{NO_3} and Z_{PO_4} were defined from the GO-SHIP data set with threshold concentrations of $[\text{NO}_3^-] = 3 \mu\text{mol kg}^{-1}$ and $[\text{PO}_4^{3-}] = 3/16 \mu\text{mol kg}^{-1}$ respectively. The difference was found using average values of Z_{NO_3} and Z_{PO_4} , such that both were deeper than 50 m deep and from 45°S - 45°N. The difference was calculated for each unique geographic coordinate and year from 1972 - 2022.

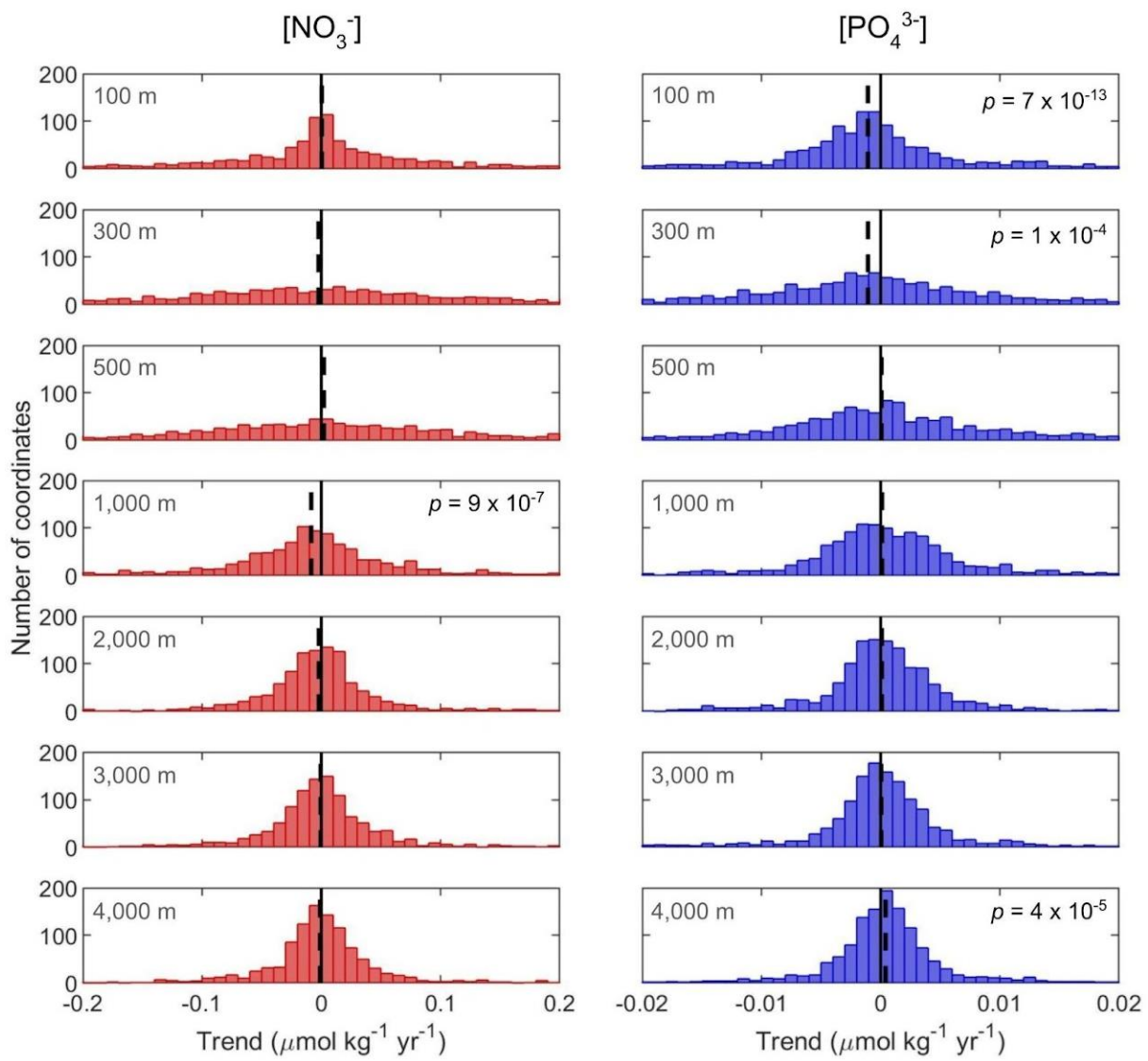


Figure S7: The difference of GO-SHIP observations and GLODAP climatology showed limited measurement bias. These histograms show the trends with time for the differences between observed nutrient concentrations in GO-SHIP and their respective climatology values in GLODAPv2.2016. Observed concentrations were averaged to each unique geographic coordinate and year. The p values from the sign test that were greater than 0.05 are not displayed.

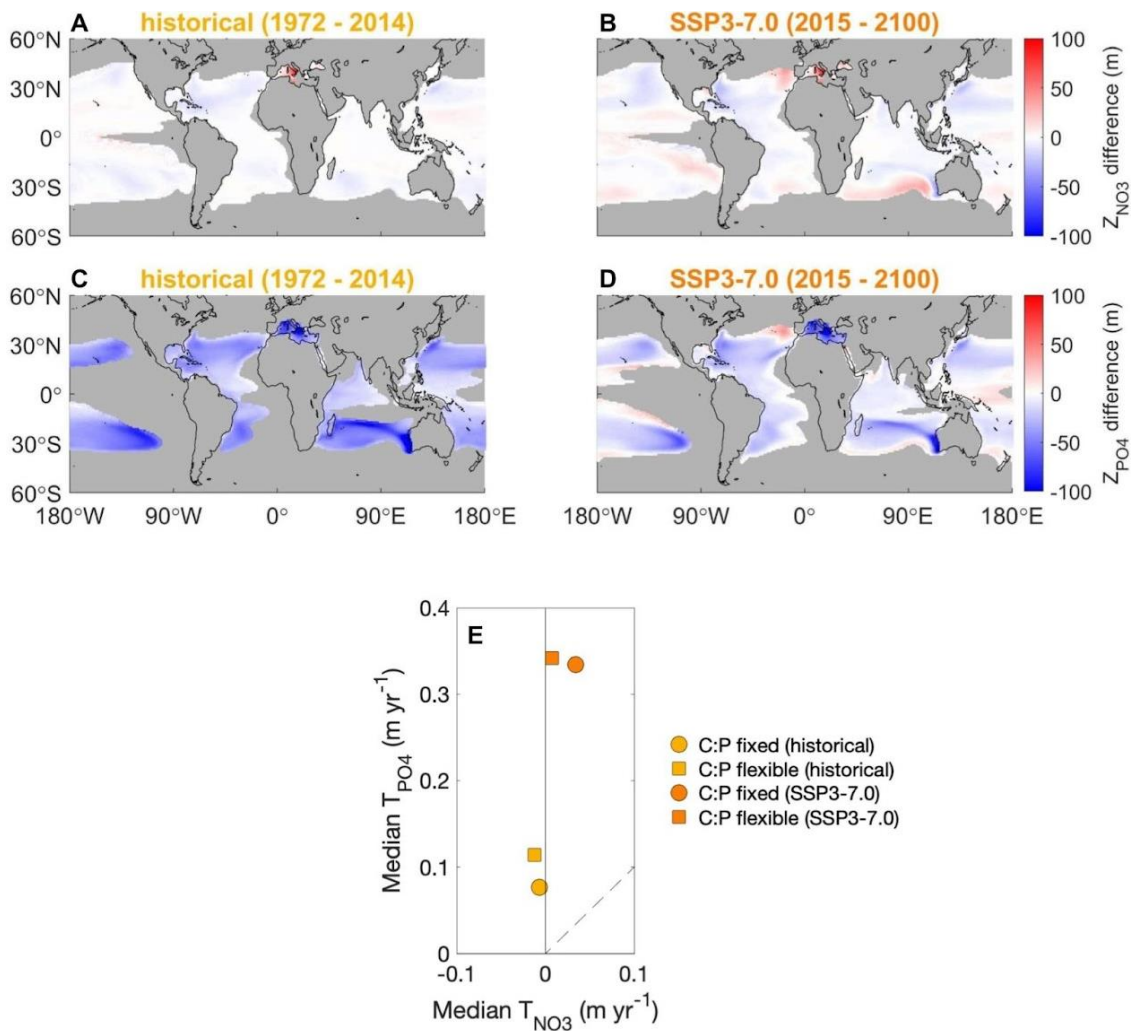


Figure S8: Flexible phytoplankton C:P in CESM2 shoaled mean phosphacline depths. We determined how flexible phosphate uptake affected nutricline trends in a CESM2 model described by Kwon et al. (2022) (37). The difference of mean Z_{NO_3} with flexible C:P and mean Z_{NO_3} with fixed (i.e., Redfield) C:P under the (A) historical and (B) SSP3-7.0 scenarios. The difference of mean Z_{PO_4} with flexible C:P and mean Z_{PO_4} with fixed C:P under the (C) historical and (D) SSP3-7.0 scenarios. Z_{NO_3} and Z_{PO_4} were defined with threshold concentrations of $[NO_3^-] = 3 \mu\text{mol m}^{-3}$ and $[PO_4^{3-}] = 3/16 \mu\text{mol m}^{-3}$, respectively. The difference calculation uses mean values of nutricline depths over the entire time period. Negative values indicate that average nutricline depths were deeper when C:P was fixed, whereas positive values indicate they were deeper when C:P was flexible. (E) Median site-specific trends of nutricline and phosphaclines for fixed and flexible C:P under both emission scenarios. The dashed line is where $T_{PO_4} = T_{NO_3}$.

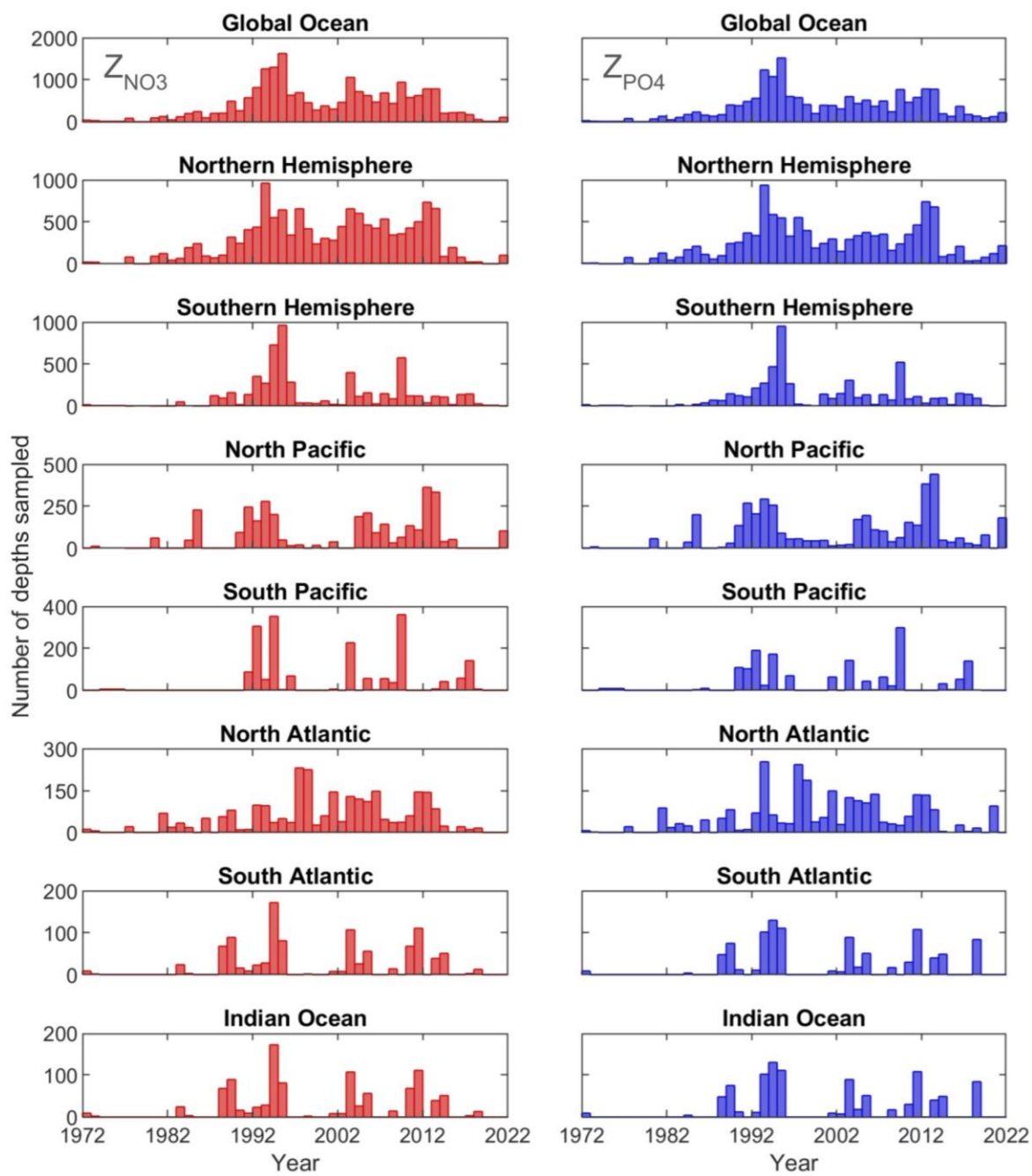


Figure S9: Z_{NO_3} and Z_{PO_4} were sampled concurrently throughout the global ocean. The histograms show the number of nitracline and phosphacline depths defined for each year. Each nutricline depth was an annual average for a unique geographic coordinate. The nutricline depths shown here were determined from the GO-SHIP data set using threshold concentrations of $[NO_3^-] = 3 \mu\text{mol kg}^{-1}$ and $[PO_4^{3-}] = 3/16 \mu\text{mol kg}^{-1}$ respectively. The boundaries defining each ocean region are described in Tables S2 and S4.

Table S1: Global regressions of nutricline depths

Data set	[NO ₃ ⁻] threshold (μmol kg ⁻¹)	[PO ₄ ³⁻] threshold (nmol kg ⁻¹)	Z _{NO₃}			Z _{PO₄}			ANCOVA p value
			Slope (m yr ⁻¹)	Slope SE (m yr ⁻¹)	Model p value	Slope (m yr ⁻¹)	Slope SE (m yr ⁻¹)	Model p value	
GO-SHIP	1	63	0.06	0.05	0.2 (n = 6,077)	0.13	0.09	0.2 (n = 2,977)	0.5
GO-SHIP	3	188	0.14	0.08	0.07 (n = 7,513)	0.47	0.10	9 x 10 ⁻⁷ (n = 6,823)	7 x 10 ⁻³
GO-SHIP	5	313	0.35	0.10	7 x 10 ⁻⁴ (n = 8,166)	0.80	0.10	6 x 10 ⁻¹⁷ (n = 8,345)	2 x 10 ⁻³
GO-SHIP (Z > 25 m)	1	63	0.25	0.06	3 x 10 ⁻⁵ (n = 7,071)	0.33	0.09	2 x 10 ⁻⁴ (n = 3,776)	0.4
GO-SHIP (Z > 25 m)	3	188	0.21	0.08	9 x 10 ⁻³ (n = 8,237)	0.53	0.09	6 x 10 ⁻⁹ (n = 7,736)	6 x 10 ⁻³
GO-SHIP (Z > 25 m)	5	313	0.47	0.11	9 x 10 ⁻⁶ (n = 8,724)	0.82	0.10	5 x 10 ⁻¹⁸ (n = 9,085)	0.01
GO-SHIP (1982 - 2012)	3	188	0.30	0.10	3 x 10 ⁻³ (n = 6,510)	0.63	0.14	3 x 10 ⁻⁶ (n = 5,637)	0.04
GLODAP	3	188	0.27	0.06	2 x 10 ⁻⁶ (n = 11,364)	0.58	0.07	6 x 10 ⁻¹⁵ (n = 8,559)	5 x 10 ⁻⁴
WOD	3	188	0.18	0.05	1 x 10 ⁻⁴ (n = 19,335)	0.35	0.06	1 x 10 ⁻⁹ (n = 13,441)	0.02

Each datapoint of a regression was an annually-averaged nutricline depth for a unique geographic coordinate vs. the year. These depths were from 45°S – 45°N, deeper than 50 m depth, and from years 1972 – 2022 unless otherwise stated in the “Data set” column. The two groups for the ANCOVA had the same sample sizes as the regression models.

Table S2: Regional depths from GO-SHIP

Region	Spatial bounds	Mean Z_{NO_3} (m)	Mean Z_{PO_4} (m)	Mean $Z_{NO_3} - Z_{PO_4}$ (m)
Global	-45°N to 45°N	123 (n = 9,317)	91 (n = 9,847)	31 (n = 9,189)
North hemisphere	1°N to 45°N	127 (n = 5,258)	116 (n = 5,416)	11 (n = 5,200)
South hemisphere	-45°N to -1°N	121 (n = 3,886)	62 (n = 4,257)	57 (n = 3,817)
North Pacific	15°N to 45°N, 120°E to -100°E	146 (n = 2,016)	116 (n = 2,091)	29 (n = 2,006)
North Atlantic	15°N to 45°N, -75°E to -10°E	138 (n = 1,509)	148 (n = 1,556)	-11 (n = 1,498)
South Pacific	-45°N to -15°N, 120°E to -70°E	155 (n = 1,181)	62 (n = 1,461)	86 (n = 1,181)
South Atlantic	-45°N to -15°N, -70°E to 20°E	119 (n = 844)	67 (n = 930)	53 (n = 842)
Indian Ocean	-45°N to -15°N, 30°E to 115°E	128 (n = 870)	75 (n = 855)	57 (n = 826)

Mean values of annually-averaged nutricline depths in the GO-SHIP data set from 1972 – 2022. The nitracline (Z_{NO_3}) and phosphacline (Z_{PO_4}) were defined from threshold concentrations of 3 $\mu\text{mol kg}^{-1}$ and 3/16 $\mu\text{mol kg}^{-1}$ for nitrate and phosphate respectively.

Table S3: Site-specific trends of nutricline depths

Data set	[NO ₃ ⁻] threshold (μmol kg ⁻¹)	[PO ₄ ³⁻] threshold (nmol kg ⁻¹)	T _{NO₃}				T _{PO₄}				Kruskal-Wallis test p value
			Median (m yr ⁻¹)	CI _{95%} (m yr ⁻¹)	MToRP two-tailed p value	Sign test p value	Median (m yr ⁻¹)	CI _{95%} (m yr ⁻¹)	MToRP two-tailed p value	Sign test p value	
GO-SHIP	1	63	-0.17	-0.27, -0.04	1 x 10 ⁻³ (n = 4,374)	5 x 10 ⁻³ (n = 1,544)	0.37	0.22, 0.50	0 (n = 2,197)	3 x 10 ⁻⁴ (n = 683)	9 x 10 ⁻⁷
GO-SHIP	3	188	-0.11	-0.22, -0.02	0.02 (n = 5,539)	0.02 (n = 1,859)	0.35	0.20, 0.49	0 (n = 5,279)	3 x 10 ⁻⁶ (n = 1,641)	8 x 10 ⁻⁷
GO-SHIP	5	313	-0.10	-0.21, 0	0.09 (n = 5,980)	0.05 (n = 1,974)	0.25	0.11, 0.37	0 (n = 6,463)	9 x 10 ⁻⁵ (n = 1,975)	2 x 10 ⁻⁵
GO-SHIP (Z > 25 m)	1	63	-0.18	-0.28, -0.05	5 x 10 ⁻⁴ (n = 5,073)	2 x 10 ⁻³ (n = 1,771)	0.45	0.32, 0.62	0 (n = 2,801)	5 x 10 ⁻⁶ (n = 878)	4 x 10 ⁻⁹
GO-SHIP (Z > 25 m)	3	188	-0.16	-0.27, -0.05	8 x 10 ⁻⁴ (n = 6,026)	2 x 10 ⁻³ (n = 2,020)	0.28	0.14, 0.43	0 (n = 5,949)	2 x 10 ⁻⁴ (n = 1,838)	1 x 10 ⁻⁷
GO-SHIP (Z > 25 m)	5	313	-0.14	-0.23, -0.04	0.01 (n = 6,333)	8 x 10 ⁻³ (n = 2,099)	0.22	0.10, 0.33	0 (n = 6,960)	2 x 10 ⁻⁴ (n = 2,139)	1 x 10 ⁻⁵
GO-SHIP (1982 - 2012)	3	188	-0.36	-0.50, -0.20	0 (n = 4,521)	3 x 10 ⁻⁶ (n = 1,662)	0.14	0.03, 0.34	0.04 (n = 4,113)	0.01 (n = 1,450)	2 x 10 ⁻⁵
GLODAP	3	188	-0.13	-0.21, -0.05	4 x 10 ⁻⁴ (n = 9,174)	2 x 10 ⁻³ (n = 2,410)	0.27	0.15, 0.40	0 (n = 6,892)	2 x 10 ⁻⁷ (n = 1,800)	7 x 10 ⁻⁹
WOD	3	188	-0.13	-0.20, -0.05	0 (n = 15,678)	2 x 10 ⁻⁴ (n = 3,781)	0.24	0.14, 0.35	0 (n = 10,882)	2 x 10 ⁻⁶ (n = 2,627)	6 x 10 ⁻¹⁰

Site-specific trends were determined from annually-averaged nutricline depths that were from 45°S – 45°N, deeper than 50 m depth, and from years 1972 – 2022 unless otherwise stated in the “Data set” column. The 95% confidence intervals (CI_{95%}) of the medians were calculated by generating 10,000 bootstrap samples of the site-specific trends. The number of annually-averaged nutricline depths used to construct 10,000 random populations are the sample size (n) in the MToRP columns. Each p value in the MToRP columns was the fraction of MToRP that had a higher absolute value than the absolute value of the median trend from the observations. The sample size for the sign test was the number of unique geographic coordinates. The two groups for the Kruskal-Wallis test had the same sample sizes as the sign tests.

Table S4: Regional trends from GO-SHIP

Region	Spatial bounds	T _{NO₃}				T _{PO₄}				Kruskal-Wallis test <i>p</i> value
		Median (m yr ⁻¹)	CI _{95%} (m yr ⁻¹)	MToRP two-tailed <i>p</i> value	Sign test <i>p</i> value	Median (m yr ⁻¹)	CI _{95%} (m yr ⁻¹)	MToRP two-tailed <i>p</i> value	Sign test <i>p</i> value	
North hemisphere	1°N to 45°N	-0.02	-0.16, 0.13	0.8 (n = 3,344)	0.8 (n = 995)	0.13	-0.05, 0.35 (n = 3,491)	0.03 (n = 982)	0.1 (n = 982)	0.3
South hemisphere	-45°N to -1°N	-0.27	-0.40, -0.09	2 x 10 ⁻⁴ (n = 2,142)	1 x 10 ⁻³ (n = 849)	0.60	0.41, 0.71 (n = 1,738)	0 (n = 643)	2 x 10 ⁻⁷ (n = 643)	5 x 10 ⁻¹¹
North Pacific	15°N to 45°N, 120°E to -100°E	-0.03	-0.26, 0.18	0.8 (n = 1,496)	0.9 (n = 422)	0.26	-0.05, 0.50 (n = 1,545)	7 x 10 ⁻³ (n = 392)	0.1 (n = 392)	0.4
North Atlantic	15°N to 45°N, -75°E to -10°E	-0.40	-0.80, -0.04	3 x 10 ⁻³ (n = 979)	0.04 (n = 312)	0.06	-0.28, 0.60 (n = 1,069)	0.8 (n = 342)	0.9 (n = 342)	0.05
South Pacific	-45°N to -15°N, 120°E to -70°E	-0.45	-0.75, -0.16	1 x 10 ⁻⁴ (n = 844)	7 x 10 ⁻⁴ (n = 346)	0.65	0.32, 0.86 (n = 614)	2 x 10 ⁻⁴ (n = 220)	2 x 10 ⁻⁴ (n = 220)	3 x 10 ⁻⁹
South Atlantic	-45°N to -15°N, -70°E to 20°E	0.06	-0.12, 0.31	0.6 (n = 438)	0.6 (n = 173)	0.72	0.52, 1.24 (n = 352)	8 x 10 ⁻³ (n = 130)	3 x 10 ⁻⁴ (n = 130)	2 x 10 ⁻³
Indian Ocean	-45°N to -15°N, 30°E to 115°E	-0.41	-0.80, 0.29	0.10 (n = 510)	0.2 (n = 210)	0.50	0.01, 0.93 (n = 503)	0.02 (n = 199)	0.07 (n = 199)	0.06

The [NO₃⁻] and [PO₄³⁻] thresholds to define Z_{NO₃} and Z_{PO₄} were 3 μmol kg⁻¹ and 3/16 μmol kg⁻¹ respectively. Site-specific trends were determined from nutricline depths deeper than 50 m depth and from years 1972 – 2022. The 95% confidence intervals (CI_{95%}) of the medians were calculated by generating 10,000 bootstrap samples of the site-specific trends. The number of annually-averaged nutricline depths used to construct 10,000 random populations are the sample size (n) in the MToRP columns. Each *p* value in the MToRP columns was the fraction of MToRP that had a higher absolute value than the absolute value of the median trend from the observations. The sample size for the sign test was the number of unique geographic coordinates. The two groups for the Kruskal-Wallis test had the same sample sizes as the sign tests.

Table S5: Residual T_{PO4} vs. ocean nitrogen fixation rates in CMIP6

Scenario	Slope (m x [Tg N _{fix}] ⁻¹)	Slope SE (m x [Tg N _{fix}] ⁻¹)	R ²	p value
historical	2.5 x 10 ⁻⁴	1.1 x 10 ⁻⁴	0.3	0.04 (n = 15)
ssp245	1.0 x 10 ⁻³	2.1 x 10 ⁻⁴	0.7	8 x 10 ⁻⁴ (n = 11)
ssp585	1.3 x 10 ⁻³	2.4 x 10 ⁻⁴	0.8	4 x 10 ⁻⁴ (n = 11)

Statistics of the linear regressions for the residual T_{PO4} vs. ocean nitrogen fixation rates across CMIP6 models.

Table S6: CMIP6 models with scenarios and variables of interest

Model	historical no3, po4, thetao & so	ssp245 no3, po4, thetao & so	ssp585 no3, po4, thetao & so	historical intpn2	ssp245 intpn2	ssp585 intpn2
ACCESS-ESM1-5	x	x	x			
CESM2	x	x	x	x	x	x
CESM2-FV2	x			x		
CESM2-WACCM	x	x	x	x	x	x
CESM2-WACCM-FV2	x			x		
CMCC-ESM2	x	x	x			
CNRM-ESM2-1	x	x	x	x	x	x
EC-Earth3-CC	x	x	x	x	x	x
GFDL-ESM4	x	x	x	x	x	x
IPSL-CM5A2-INCA	x					
IPSL-CM6A-LR	x	x	x	x	x	x
IPSL-CM6A-LR-INCA	x			x		
KIOST-ESM	x	x	x			
MIROC-ES2H	x	x	x			
MIROC-ES2L	x	x	x	x	x	x
MPI-ESM-1-2-HAM	x			x		
MPI-ESM1-2-HR	x	x	x	x	x	x
MPI-ESM1-2-LR	x	x	x	x	x	x
MRI-ESM2-0	x		x			
NorESM2-LM	x	x	x	x	x	x
NorESM2-MM	x	x	x	x	x	x
UKESM1-0-LL	x	x	x			

Variables available in each model and scenario are denoted by an “x.” Ocean temperature is “thetao,” salinity is “so,” and nitrogen fixation is “intpn2.” Model variables were from the r1i1p1f1 experiment version if it was available.